The Kinetochore Protein KNL-1 Regulates the Actin Cytoskeleton to Control Dendrite Branching

Mattie Green[1], Henrique Alves Domingos [1], Vasileios R. Ouzounidis [1], Cameron Finlayson[1], Bram Prevo[1] & Dhanya K. Cheerambathur [1]*

[1]Wellcome Centre for Cell Biology & Institute of Cell Biology, School of Biological Sciences, The University of Edinburgh, Edinburgh, EH9 3BF, UK

* Corresponding author

ABSTRACT

The function of the nervous system is intimately linked to its complex and highly inter-connected architecture. Precise control of dendritic branching in individual neurons is central to building the complex structure of the nervous system. Here we show that the kinetochore protein KNL-1 and its associated KMN (Knl1/Mis12/Ndc80 complex) network partners, typically known for their role in chromosome-microtubule coupling during mitosis, regulate dendrite branching in the *C. elegans* mechanosensory PVD neuron. KNL-1 restrains excess dendritic branching and promotes contact-dependent repulsion events, ensuring robust sensory behaviour and protecting against age-dependent neuron degeneration. Surprisingly, KNL-1 does not act via modulating the microtubule cytoskeleton in dendrites. Instead, KNL-1 controls the actin cytoskeleton to ensure proper dendrite architecture. These findings establish that the post-mitotic neuronal KMN network acts to shape the developing nervous system by regulating the actin cytoskeleton and provide new insight into the mechanisms controlling dendrite architecture.

INTRODUCTION

Neurons have specialized compartments for transmitting information, including dendrites, which receive & integrate signals, and axons, which relay them. The shape, size and trajectory of dendritic and axonal processes determines how a neuron communicates and functions. Dendrites display diverse shapes and complex branching patterns that are unique to neuronal types(Jan and Jan, 2001; Lefebvre et al., 2015). The dendrite arborization pattern defines how input signals are distributed and integrated, ultimately shaping the functional properties of neurons and their connectivity within neural circuits. Proper development and organization of dendritic arbors is therefore crucial for establishing the neural circuits that regulate animal behavior. Notably, alterations in dendrite morphology and organization are associated with neurodevelopmental and neurodegenerative disorders(Jan and Jan, 2010).

Dendrite morphogenesis initiates when extrinsic guidance cues interact with specific cell surface receptors on the neuron and activate intracellular signaling pathways that trigger cytoskeletal rearrangements to enable dendrite growth and branching(Jan and Jan, 2010; Lefebvre, 2021). The Rho family of GTPases (Cdc-42, Rac1, and RhoA) are key downstream effectors of the guidance cues during dendrite development(Li et al., 2000; Luo et al., 1996; Threadgill et al., 1997; Nakayama et al., 2000). During dendrite outgrowth, dynamic actin filaments form a network of lamellipodial and filopodial protrusions that guide and propel the growth cone. Rho GTPases influence dendrite arborization by regulating actin filament assembly and the formation of actin structures such as filopodia and lamellipodia. Dendritic arborization occurs when filopodia emerge from preexisting branches and undergo cycles of extension and retraction until they become stabilized(Scott and Luo, 2001). Consequently, dendrite arbor growth and stabilization entail extensive actin remodeling and careful coordination between actin growth states and structures. Various actin regulators, including F-actin nucleators and

modulators of F-actin dynamics, have been shown to affect dendrite morphogenesis(Sundararajan et al., 2019b; Ouzounidis et al., 2023). However, it is unclear how the activity of different actin regulators is coordinated and controlled spatially and temporally to generate a specific dendrite pattern.

The microtubule cytoskeleton is also critical for dendrite morphogenesis. Microtubules provide structural support for dendrites and serve as tracks to transport key building materials and organelles. Mutations in molecular motors that affect transport severely impair dendrite morphology, and loss of microtubule-associated proteins results in dendrite development defects(Taylor et al., 2015; Maniar et al., 2012; Jaworski et al., 2009; Cao et al., 2020; Kahn et al., 2018). In addition, microtubule nucleators are found at branch points of developing dendrites, where they organize microtubule arrays to regulate branching(Nguyen et al., 2014). Studies of the role of microtubules in dendritic spines, small actin-rich protrusions on dendrite branches that are sites of high synaptic activity, have shown that dynamic microtubules enter the actin-rich spines in a synaptic-activity-dependent manner and that this is facilitated by actin cytoskeleton remodeling(Jaworski et al., 2009; Merriam et al., 2011; Hu et al., 2008). Thus, a crosstalk between the two cytoskeletal networks appears to exist within dendrites, but its molecular basis remains elusive.

Recent studies have revealed that kinetochore proteins, which connect chromosomes to dynamic spindle microtubules in dividing cells, also play an unexpected post-mitotic role during neurodevelopment. The conserved 10-subunit Knl1 complex/Mis12 complex/Ndc80 complex (KMN) network, which serves as the primary chromosome-microtubule coupler in mitosis(Musacchio and Desai, 2017), is enriched along developing dendrites of *C. elegans* sensory neurons and in the synapses and axons of *D. melanogaster* neurons(Cheerambathur et al., 2019; Zhao et al., 2019). Depletion of any KMN component in *C. elegans* sensory neurons results in dendrite growth defects,

indicating that KMN function is critical for dendrite development(Cheerambathur et al., 2019). Knockdown of Mis12 causes dendrite branching defects in *D. melanogaster* embryonic sensory neurons and increases filopodial protrusions in dendrites of rat hippocampal neurons, underscoring the importance of the Mis12 complex for proper dendrite formation(Zhao et al., 2019). Moreover, kinetochore proteins promote dendrite regeneration of *D. melanogaster* sensory neurons, highlighting their involvement in the maintenance of dendrite morphology(Hertzler et al., 2020).

The mechanisms by which kinetochore proteins contribute to dendrite development and maintenance is not well understood, but some observations imply that microtubule binding activity is important(Cheerambathur et al., 2019; Hertzler et al., 2020). The neuronal function of the KMN network in *C. elegans* sensory neurons depends on the microtubule coupling interface within the Ndc80 complex. Additionally, knockdown of kinetochore proteins in *D. melanogaster* sensory neurons increases the number of microtubule plus ends in dendrites, suggesting a role in the regulation of microtubule dynamics (Hertzler et al., 2020).

Our previous characterization of the KMN network's post mitotic role in neurons focused on dendrite extensions of the *C. elegans* amphid sensory neuron bundles, which consist of dendrites from 12 neurons(Cheerambathur et al., 2019). This precluded a detailed analysis of cellular structures within dendrites at the single-neuron level. To overcome this limitation, here we examine the role of the KMN network component KNL-1 during dendrite branching of the mechanosensory neuron PVD. Dendrite development in PVD is stereotypical and invariant, and its cytoskeletal organization is well characterized, making it a good system to investigate kinetochore protein function. We demonstrate that KNL-1 is concentrated in the extending dendrites processes and at branch points, and that PVD-specific degradation of KNL-1 perturbs higher order branch formation, leading to behavioral defects and premature neurodegeneration. Surprisingly,

KNL-1 degradation does not affect microtubule organization or dynamics, but instead up-regulates F-actin assembly in the cell body and primary dendrites. Thus, the kinetochore protein KNL-1 contributes to the dendrite guidance pathway through regulation of the neuronal actin cytoskeleton.

RESULTS

KNL-1 localizes to developing dendrites in the PVD neuron

The PVD neuron in *C. elegans* is a type of mechanosensory neuron located between the body wall muscle and the epidermis of the animal. A unique feature of the PVD is the highly arborized dendrites that extend throughout the animal's body **(Fig. 1A)**. PVD dendrites form a distinctive branching pattern composed of non-overlapping repeating units called "menorahs", which are important for integrating and processing sensory inputs **(Fig. 1A)** (Smith et al., 2010; Oren-Suissa et al., 2010; Halevi et al., 2002; Tsalik et al., 2003). PVD dendrite branches are established during the larval stages and the branching follows a stereotypical developmental program that begins at the late L2 larval stage and concludes by the late L4 larval stage **(Fig. S1A)**. To visualize the localization of the kinetochore protein KNL-1 in the PVD neuron, we used a split-GFP system (Kamiyama et al., 2016). The N-terminus of KNL-1 was fused to 7 copies of the β11 strand of GFP at the endogenous locus, and the complementing GFP 1-10 was expressed under the *unc-86* promoter, which is active in the PVD neuron. The cell body of PVD is located near the animal tail, and two primary (1°) dendrites extend from the cell body towards the anterior and posterior of the animal. KNL-1 was enriched in the cell body and along the extending 1° dendrites at the L2 larval stage **(Fig. 1B)**. During the L3 and L4 stages, higher order branches develop from 1° dendrites to generate the distinctive menorah shape. KNL-1 signal persisted along the 1° dendrites in the L3 and L4 stages but became more punctate **(Fig. S1B)**. We also observed discrete KNL-1 puncta at the base of branch points of

secondary (2°) and tertiary (3°) dendrites, as well as along the newly formed 3° dendrites **(Fig. 1C, 1D, S1C and S1D)**. These results indicated that KNL-1 is present in developing PVD neurons and localized in a manner consistent with playing a role in PVD dendrite formation.

KNL-1 and other KMN network components act to restrict dendritic branching

To investigate the function of KNL-1 in the PVD neuron, we utilized an auxin inducible degron (AID) to selectively degrade KNL-1 in the PVD neuron (KNL-1 DEG). We fused an AID peptide sequence along with GFP to KNL-1 at the endogenous locus and expressed the plant specific F-box protein TIR1 under PVD-specific promoters using the Mos1-mediated single copy insertion system **(Fig. 2A)**(Ashley et al., 2021). To degrade KNL-1, we synchronized the worms as L1 larvae and exposed them to auxin at the L2 larval stage when PVD development is initiated **(Fig. S2A)**. We observed a significant reduction in GFP::KNL-1 signal from the PVD cell body at the late L2 stage **(Fig. 2A)**. To assess the effect of KNL-1 degradation on PVD development, we visualized dendrite morphology in L4 larvae expressing a plasma membrane (pleckstrin homology domain, PH) marker within the PVD neuron. In both control animals, which expressed the TIR1 transgenes in untagged KNL-1 background, and KNL-1 degrader animals the 1° dendrites of the PVD neuron extended properly**.** However, we observed a significant disruption of the higher-order branching pattern following KNL-1 degradation **(Fig. 2B and S2G)**. Menorahs consist of dendrite branches that are arranged at right angles with respect to each other. Specifically, each menorah contains a secondary (2°) dendrite that branches off at a right angle from the 1° dendrite, which then gives rise to an orthogonal 3° branch that forms the base of menorah. Finally, several smaller quarternary (4°) dendrites emerge at right angles to the 3° dendrite to complete the menorah. The number of 2° dendrite branches was not significantly different between control and KNL-1 degrader neurons **(Fig. S2B).**

However, KNL-1 degrader neurons exhibited an increased number of 4° dendrite branches **(Fig. 2C)**, an increased appearance of overlaps between 3° dendrites **(Fig. 2D)**, and an increased number of ectopic neurites originating from the 1° dendrites **(Fig. S2C)**.

We next overexpressed KNL-1 in the PVD neuron by generating extrachromosomal arrays that contain multiple copies of transgenic KNL-1::GFP under a PVD-specific promoter. Compared to control animals that contained a GFP-expressing plasmid in the array, animals with KNL-1::GFP arrays exhibited a decrease in higher-order branching. Specifically, the number of 2° and 4° dendrite branches were significantly reduced **(Fig. 2E, 2F and S2D)**. We conclude that PVD-specific degradation and overexpression of KNL-1 have opposite effects on higher-order dendritic branching.

We also investigated the effect of degrading the Mis12 and the Ndc80 complexes within the KMN network on PVD branching. Degradation of KNL-3 (a component of the Mis12 complex) or NDC-80 subunit of the Ndc80 complex disrupted PVD dendrite architecture in a similar manner to KNL-1 degradation **(Fig. S2C and S2F-S2I)**. Taken together, these results reveal that PVD-localized KNL-1 functions in the context of the KMN network to restrict dendritic branching. We conclude that the kinetochore-microtubule coupling machinery has a critical role in ensuring proper PVD dendrite arborization.

KNL-1 regulates contact-dependent repulsion between dendrite branches

A prominent effect of KNL-1 degradation is the appearance of fusion between neighboring menorahs resulting from the merge or overlap of 3° dendrites **(Fig. 2G)**. In control neurons, 3° dendrites of neighboring menorahs do not overlap with each other as they quickly retract after contacting each other through a phenomenon termed contact-dependent dendritic self-avoidance(Smith et al., 2012). The increase in aberrant overlapping menorahs observed following KNL-1 degradation **(Fig. 2D)** and the presence

of GFP::KNL-1 puncta along the 3° dendrite and at branch points within the menorah **(Fig. 1C and S1D)** suggests that KNL-1 plays a role in resolving contacts between the growing tips of neighboring 3° dendrites. To understand how KNL-1 contributes to the spatial separation of menorahs, we tracked the growth dynamics of 3° dendrites. Consistent with previous studies(Smith et al., 2010; Liao et al., 2018; Smith et al., 2012), 3° dendrites of neighboring menorahs retracted within 5-10 min of mutual contact in control neurons **(Fig. 2G-2I)**. In KNL-1 degrader neurons, the frequency with which neighboring 3° dendrites established contact remained unchanged **(Fig.S2E)** but contact duration was longer **(Fig. 2I)**. The presence of persistent contacts after KNL-1 degradation resulted in a higher frequency of unresolved contacts, indicating that KNL-1 function ensures timely retraction of 3° dendrites during menorah formation **(Fig. 2H)**. These observations suggest that KNL-1 regulates the growth dynamics of dendrite branches. Specifically, KNL-1 activity is required for the 3° dendrites to undergo contact-dependent dendritic self-avoidance, essential for spatial patterning of dendrite branches in the PVD neuron.

KNL-1 degradation does not perturb PVD polarity, microtubule organization, or microtubule dynamics

Next, we explored the mechanism by which KNL-1 inlfuences dendrite branching. The canonical role of KMN network proteins is to mediate dynamic interactions between chromosomes and microtubules during chromosome segregation. Therefore, we hypothesized that KNL-1 affected PVD dendrite branching by regulating the underlying microtubule stability and architecture. Since microtubule function is critical for the establishment and maintenance of neuronal polarity in the PVD neuron, we first tested whether degradation of KNL-1 impacts neuronal polarity(He et al., 2020, 2022; Maniar et al., 2012). To determine whether KNL-1 degradation impacts PVD polarity, we assessed the distribution of RAB-3, a small GTPase associated with synaptic vesicles, and DMA-1,

which localizes exclusively to dendrites **(Fig. 3A)**. We observed no change in the distribution of either RAB-3 or DMA-1 following KNL-1 degradation, indicating that PVD polarity remains intact **(Fig. 3B, 3C, S3A and S3B)**.

Next, we investigated whether KNL-1 degradation impacts the distribution, dynamics, or stability of microtubules in the 1° anterior dendrite. To monitor microtubule orientation and dynamics we imaged the microtubule plus end-tracking protein $EB1^{EBP-2}$, which binds to growing microtubule plus ends. $EB1^{EBP-2}$::GFP was expressed under a PVD-specific promoter, and its trajectories were followed by time-lapse imaging in L4 larvae **(Fig. 3D)**. In control neurons, the majority of the $EB1^{EBP-2}$::GFP puncta moved towards the cell body, which is consistent with previous observations (Harterink et al., 2018; Taylor et al., 2015; He et al., 2020, 2022) that within the 1° anterior dendrite microtubules are oriented with their minus end distal **(Fig. 3D and 3E)**. There was no significant difference in the direction of movement, velocity, or frequency of $EB1^{EBP-2}$::GFP comets in KNL-1 degrader neurons **(Fig. 3D, 3E, S3D and S3E)**. Thus, KNL-1 does not contribute to the orientation, distribution, or dynamics of microtubule plus ends within PVD dendrites.

We also examined tubulin distribution and microtubule stability in PVD dendrites by expressing an α-tubulin GFP-fusion protein. GFP::TBA-1 is enriched in 1° dendrites and is also observed in 2° and 3° dendrite branches. Both control and KNL-1 degrader animals showed a similar distribution of GFP::TBA-1 **(Fig. S3C)**. To assess the stability of microtubules, we performed Fluorescence Recovery After Photobleaching (FRAP) experiments on microtubules labeled with endogenous GFP::TBA-1 using the split-gfp system **(Fig. 3F)**. After KNL-1 degradation, microtubules within the 1° anterior dendrite recovered to a similar extent (~20%) and with the same kinetics as microtubules in control neurons **(Fig. 3F and S3F)**. Recovery kinetics indicate that microtubules in the 1° anterior dendrite are largely stable, and that microtubule stability is not impaired by KNL-1

degradation. Overall, these experiments indicate that neither altered neuronal polarity nor perturbed microtubule organization and dynamics account for the striking effect of KNL-1 loss on PVD dendritic branching and consequent impairment of PVD neuron function and lifespan.

KNL-1 limits F-actin assembly and dynamics in the PVD cell body and dendrites

During our morphological analysis, we noticed that the cell body in KNL-1 degrader PVD neurons was enlarged and deformed **(Fig. 4A and 4B).** Notably, prior studies have reported analogous deformations to cell bodies in response to disruptions in the RhoGTPase and actin regulatory pathways in *C. elegans* neurons, suggesting potential defects associated with the actin cytoskeleton in KNL-1 degrader animals(Demarco et al., 2012; Leeuwen et al., 1997). To visualize the actin cytoskeleton during PVD dendrite branching, we generated a strain expressing Lifeact, the actin binding peptide of the yeast protein Abp140, fused to mKate2 under a PVD-specific promoter(Riedl et al., 2008). We imaged actin and the plasma membrane of the PVD neuron at the L4 stage, when 4° dendritic branches are forming. In control neurons, Lifeact::mKate2 signal is enriched in the 3° and 4° dendrites compared to the 1° dendrites and the cell body, consistent with previous observations(Zou et al., 2018; Tang et al., 2019; Shi et al., 2021; Zhao et al., 2022) that newly formed dendrites show a higher concentration of F-actin **(Fig. 4C)**. In KNL-1 degrader neurons, Lifeact::mKate2 signal intensity in the cell body and proximal 1° dendrites was significantly increased **(Fig. 4C),** and close examination revealed prominent F-actin cables in the cell body of KNL-1 degrader neurons **(Fig. 4D-4G)**. These results suggest that degradation of KNL-1 during PVD development results in an overall increase of F-actin levels inside and in regions proximal to the cell body.

To assess F-actin dynamics, we performed FRAP in the 1° anterior dendrite. In both control and KNL-1 degrader neurons, recovery of Lifeact::mKate2 signal was slow

suggesting a low turnover rate for F-actin. However, the extent of recovery was significantly lower in KNL-1 degrader neurons (8% vs. 14% in controls) indicative of a higher fraction of stable F-actin structures **(Fig. 4H and 4I)**. Consistent with a role for KNL-1 in regulating F-actin dynamics, we found that KNL-1 influences the dynamics of filopodial protrusions from 1° dendrites. 2° dendrite branches initiate when several actin-rich filopodial like projections extend orthogonally from the 1° dendrite. Most of these filopodia undergo several cycles of extension and retraction until a subset of projections stabilize to form the 2° dendrites **(Fig. S3G)**. The number of filopodial protrusions from 1° dendrites was significantly increased in KNL-1 degrader neurons **(Fig. 4J, 4K and S4D)**. Unlike the filopodial outgrowths in control dendrites, which extend orthogonally for a short period, protrusions in KNL-1 degrader dendrites had a longer lifetime and arbitrary trajectories, often running parallel to 1° dendrites **(Fig. S3G)**. These observations suggest that KNL-1 plays a critical role in regulating filopodial generation and dynamics in 1° dendrites.

KNL-1 degradation impairs function and lifespan of the PVD neuron

Next, we wanted to determine the functional consequence of KNL-1 mediated actin misregulation and dendrite patterning defect on PVD function and maintenance. Proper dendrite arborization is essential for the sensory function of the PVD neuron(Liu and Shen, 2011). Hence, we examined the effect of KNL-1 on two distinct sensory behaviors, proprioception and harsh touch response attributed to the PVD neuron(Albeg et al., 2011; Way and Chalfie, 1989). Proprioception pertains to awareness of body position and movement, and the PVD dendrites sense mechanical stimuli and provide feedback to the body wall muscles to generate a stereotypical sinusoidal locomotory pattern **(Fig. 5A)**. To determine the body posture of animals, we visualized their movement on food and measured wavelength and amplitude of their sinusoidal tracks. As a positive control, we included animals lacking DMA-1, a transmembrane receptor that is essential for PVD

dendrite formation and is required for proper locomotion(Tao et al., 2019). Similar to Δ*dma-1*, KNL-1 degrader animals showed reduced amplitudes and wavelengths, indicating that degradation of KNL-1 in the PVD neuron impairs proprioception **(Fig. 5B and 5C)**. We next compared the ability of control and KNL-1 degrader animals to respond to high-threshold mechanical stimuli applied to the midbody (harsh touch). In *C. elegans*, PVD in conjunction with touch receptor neurons is required for harsh touch response(Way and Chalfie, 1989). Therefore, we evaluated PVD's harsh touch response in *mec-4* mutant background, which eliminates the touch receptor function(Liu and Shen, 2011). In contrast to control animals, a significant percentage of KNL-1 degrader animals displayed defective touch response **(Fig. 5D)**. The results of the behavioral assays indicate that KNL-1 ensures appropriate behavioral responses linked to the PVD neuron.

In addition to the sensory defects, we noticed morphological aberrations in the PVD architecture which were indicative of degenerating neuron(Pan et al., 2011; E et al., 2018). Specifically, at the L4 stage the dendrites of KNL-1 degrader neurons contained more bead-like structures compared to control neurons **(Fig. 5E and 5F)**. Beading or bubble like lesions along axons and dendrites are morphological defects that have been previously shown to be associated with age-dependent decline of neurons in *C. elegans*(E et al., 2018; Pan et al., 2011). In PVD dendrites, extensive beading does not appear until late into adulthood (Day 6) in control neurons. The presence of substantial beading at the L4 stage suggested that KNL-1 degrader neurons may degenerate prematurely. Age-dependent degeneration of PVD dendrites is mediated by the autophagy pathway(E et al., 2018), and autophagosomes marked by mScarlet-I::LGG-1, driven under PVD-specific *des-2* promoter, were enriched in dendrites of KNL-1 degrader neurons at the day 1 adult stage **(Fig. 5G and 5H)**. These observations suggest that KNL-1 degradation predisposes the PVD neuron to premature ageing. Taken together, the above findings highlight that

KNL-1 function in the PVD neuron is essential for the neuron's ability to function properly as well as maintain its lifespan.

DISCUSSION

Dendrite morphogenesis is a highly orchestrated process that requires precise regulation of the actin and microtubule cytoskeleton. Various effectors of cytoskeletal remodeling in dendrites have been identified, but how effector functions are coordinated to generate the unique dendrite pattern of each neuron remains largely undefined. Taking advantage of the remarkable stereotypical morphology of the PVD neuron and using a PVD-specific protein-degradation system, we identified a role for the KMN network, the microtubule-coupling machine that drives chromosome segregation during cell division, in dendrite arborization. Specifically, our work shows that KNL-1, the scaffold for microtubule and spindle assembly checkpoint machinery at the kinetochore, controls PVD dendrite branch organization and dynamics, and that KNL-1 function is essential for proper sensory behavior as well as normal ageing of the PVD neuron. We traced the source of dendrite patterning defects associated with loss of KNL-1 to attenuation of contact-dependent retraction events, a developmental mechanism that establishes optimal spacing and coverage of dendritic fields(Lefebvre et al., 2015). Additonally, we showed that loss of KNL-1 impacts the actin cytoskeleton rather than the microtubule cytoskeleton within the PVD neuron. Specifically, an increased level of filamentous actin was observed in the absence of KNL-1 while microtubule dynamics remained unchanged.

Surprisingly, our work demonstrates that KNL-1 degradation leads to increased F-actin levels in the cell body and primary dendrites and promotes formation of filopodial protrusions from primary dendrites, suggesting that KNL-1 might control actin filament dynamics. Although unexpected ,knockdown of Mis12, another KMN component, in rat hippocampal neurons resulted in an increase in filopodial protrusions, consistent with the

idea that KMN proteins may also affect the actin cytoskeleton(Zhao et al., 2019). While a direct connection between the KMN network and the actin cytoskeleton has not yet been described, several clues suggest a potential link between the actin machinery and kinetochores in the context of chromosome-microtubule attachment during cell division. Previous work has shown that the formin mDia3, a nucleator of linear actin filaments, is enriched at kinetochores of T98G glioblastoma cells and that it contributes to the stability of kinetochore-attached microtubules(Cheng et al., 2011; Yasuda et al., 2004). Moreover, the actin cytoskeleton is crucial for the formation of kinetochore-microtubule fibres during mammalian oocyte meiosis and F-actin cables generated by formin and spire, another nucleator of linear actin filaments, have been shown to interact with kinetochores during porcine oocyte meiosis(Harasimov et al., 2023; Mogessie and Schuh, 2017). PVD dendrite branching is a collaborative effort between branched actin filaments generated by the Arp2/3 complex and factors responsible for linear actin filament assembly(Shi et al., 2021; Liao et al., 2018; Sundararajan et al., 2019b). In the KNL-1 degraded animals we observe an increase in filopodia and in the number of higher order quarternary branches whereas overexpression leads to fewer branches. Based on these observations we propose that KNL-1 modulates the activity of either the regulators of branched actin or those of linear actin to influence the actin filament dynamics during dendrite branching.

One of the striking defects following the degradation of KMN proteins is the occurrence of overlapping menorahs, in which tertiary dendrites appear to be fused. This observation implies that KMN activity is not necessary for dendrite branch growth but plays an important role in spatial patterning of the dendrite branches or dendritic self-avoidance mechansims. The shaping and organization of dendrites for optimal coverage of the dendritic field have significant implications for neuronal information processing(Lefebvre et al., 2015). The development of non-overlapping arbors is a result of contact-dependent self-avoidance mediated by cell surface receptor-ligand interactions between dendrite

branches of the same neuron(Lefebvre et al., 2015). The specific molecules that act downstream of the cell surface receptors to facilitate contact-dependent retraction events responsible for dendritic self-avoidance remains poorly characterized. Recent studies suggest that formation of non-overlapping menorahs within the PVD neuron results from a balance of F-actin-dependent dendrite growth and retraction(Liao et al., 2018; Sundararajan et al., 2019a). Our time-lapse analysis shows that in the absence of KNL-1 the ability of tertiary dendrites to retract upon contact is compromised. An emerging view is that a balance between linear and branched actin filaments underlies the transition from extension to retraction of the growing 3° dendrites(Sundararajan et al., 2019a). However the precise molecular mechanism that trigger this transition is not known. Intriguingly, genetic evidence suggests that mutations in regulators of both linear and branched actin polymerization impair contact-dependent retraction(Liao et al., 2018; Sundararajan et al., 2019a). Our findings strongly indicate that KNL-1 plays a central role in contact-dependent retraction, and given its impact on actin dynamics in the PVD neuron, it is tempting to speculate that KNL-1 is involved in activating the specific actin machinery responsible for triggering retraction. Consequently, these observations suggest that function of KNL-1 in PVD neurons is to promote the balance between linear and branched F-actin filaments required for proper dendrite arborization.

Whether the effect of KMN network on dendrite branching and actin requires association with the microtubules remains to be determined. We show that degradation of the Ndc80 complex, which provides the primary microtubule binding activity in KMN, results in PVD dendrite branching defects similar to those observed after KNL-1 degradation. This suggests that the interaction of the KMN network with microtubules could be important for PVD branching. However, KNL-1 degradation does not appreciably affect overall microtubule organization or growth dynamics in PVD dendrites, nor does it affect PVD polarity. These observations are consistent with our prior work, where we did

not detect changes to microtubule polarity following KNL-1 degradation in the developing dendrites of amphid neurons(Cheerambathur et al., 2019). Additionally, these findings align with the observations in *D. melanogaster* larval sensory neurons where knockdown of Ndc80 and Mis12 subunits, both components of KMN network, did not not cause considerable changes in microtubule growth dynamics or microtubule stability in the dendrites(Hertzler et al., 2020). KNL-1 also does not appear to be specifically enriched at microtubule-based structures in these neurons (data not shown), and fluorescence microscopy suggests microtubule distribution is not altered in 3° and 4° dendrites of KNL-1 degraded animals **(Fig. S3C)**. Furthermore, KNL-1 function also appears to differ significantly from that of other known microtubule-associated proteins in PVD, whose inhibition primarily affects microtubule organization, growth dynamics, or neuronal polarity(He et al., 2020, 2022; Taylor et al., 2015; Yan et al., 2013). Taken together, our results argue against the idea that KNL-1 regulates the microtubule cytoskeleton in the dendrites. Neverthless, we cannot rule out the possibility that a more localized regional disruption of microtubule organization or dynamics occurs in the primary and tertiary dendrite branches in the absence of KMN components. Actin cytoskeletal dynamics is known to be influenced by microtubule cytoskeleton at structures such as focal adhesions (Seetharaman and Etienne-Manneville, 2019). Therefore, microtubules could potentially play a role in F-actin regulation during PVD dendrite branching, and KMN components may mediate such crosstalk.

An important avenue for future investigation involves identification of the actin regulators that KNL-1 acts on to influence dendrite branching mechanisms. For instance, given the close link between kinetochores and formin during chromosome segregation(Harasimov et al., 2023), an attractive hypothesis to be tested in the future is whether the PVD-localized KMN network might govern the assembly of linear F-actin through the regulation of formin-based actin nucleators. The assembly and disassembly

of actin filaments in response to external cues during dendrite branching are mediated by Rho family GTPases(Jan and Jan, 2010). Thus, another potential model to test is that KMN proteins affect actin dynamics by influencing the activity of specific Rho GTPases. Intriguingly, Cdc42, a Rho GTPase family member, is found at the centromeres and is implicated in kinetochore-microtubule attachment and is a potential candidate for further investigation(Lagana et al., 2010). Futher work is needed to determine the critical actin regulator that interfaces with the KMN network during dendritic branching.

In addition, our work shows that beyond dendrite arborization, KNL-1 activity is required for sensory behavior and to prevent premature degeneration of neurons. Importantly, reduced dendrite arborization and dendrite degeneration are hallmarks of neuronal aging and neurodegenerative disease(Emoto et al., 2016). While the mechanisms by which dendrite shape impact dendrite and neuronal lifespan are still open questions, our discovery links modulation of actin cytoskeletal dynamics by kinetochore components to these important aspects of neuronal biology.

Figure 1
Green et al.

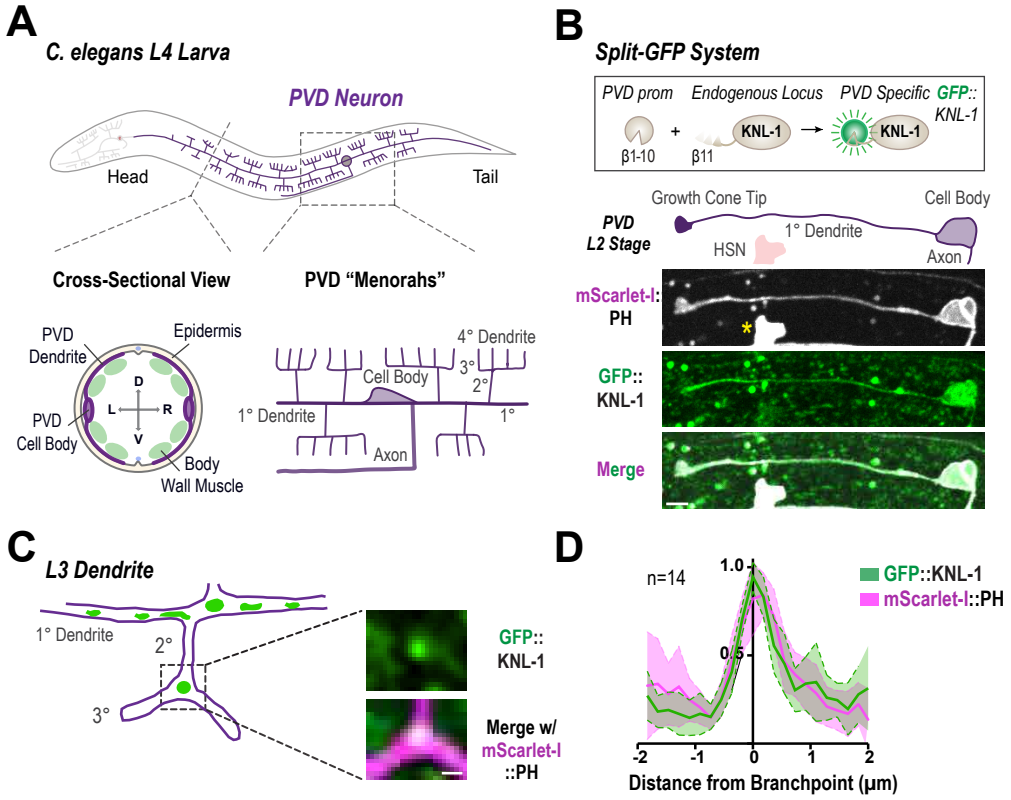

Figure 1: KNL-1 localization in the PVD neuron.

(A) Schematic of the PVD neuron at the L4 larval stage (top). The left inset cartoon shows a cross-sectional view of PVD between the epidermis and body wall muscle. The right inset illustrates the discrete "menorah" like dendrite branching pattern of PVD neuron. The two primary (1°) branches emanate in both anterior and posterior directions from the cell body, while the higher-order branches emerge perpendicularly from the pre-existing ones. The axon of the PVD extends ventrally from the cell body and incorporates into the ventral nerve cord. The dendritic branching of the PVD is completed by the end of the L4 larval stage. **(B)** Schematic of split-GFP system used to express KNL-1 in the PVD neuron during the development of the neuron (top). The images below show membrane labelled with mScarlet-I fused to the Pleckstrin Homology (PH) domain of rat PLC1δ1 (magenta) and GFP:KNL-1 (green) within the developing dendrite at the L2 larval stage. The yellow star represents GFP::KNL-1 in the cell body of HSN, another neuron where the *unc-86* promoter is active. Scale bar, 5µm. **(C)** The cartoon on the left represents the localization of GFP::KNL-1 in the dendrite branches and specifically at the branchpoint, between the 2° and 3° branches. Images of GFP::KNL-1 puncta (green) at the branch point (magenta) in the PVD dendrite at the L3 larval stage (right). Scale Bar 1µm. **(D)** Quantification of GFP::KNL-1 at the intersections of 2° and 3° dendrites as shown in (C). n represents number of animals. Dotted lines and shaded region represent mean ± SEM. Branchpoints show an increased intensity of both the membrane (PH) and KNL-1 signal.

Figure 2

Green et al.

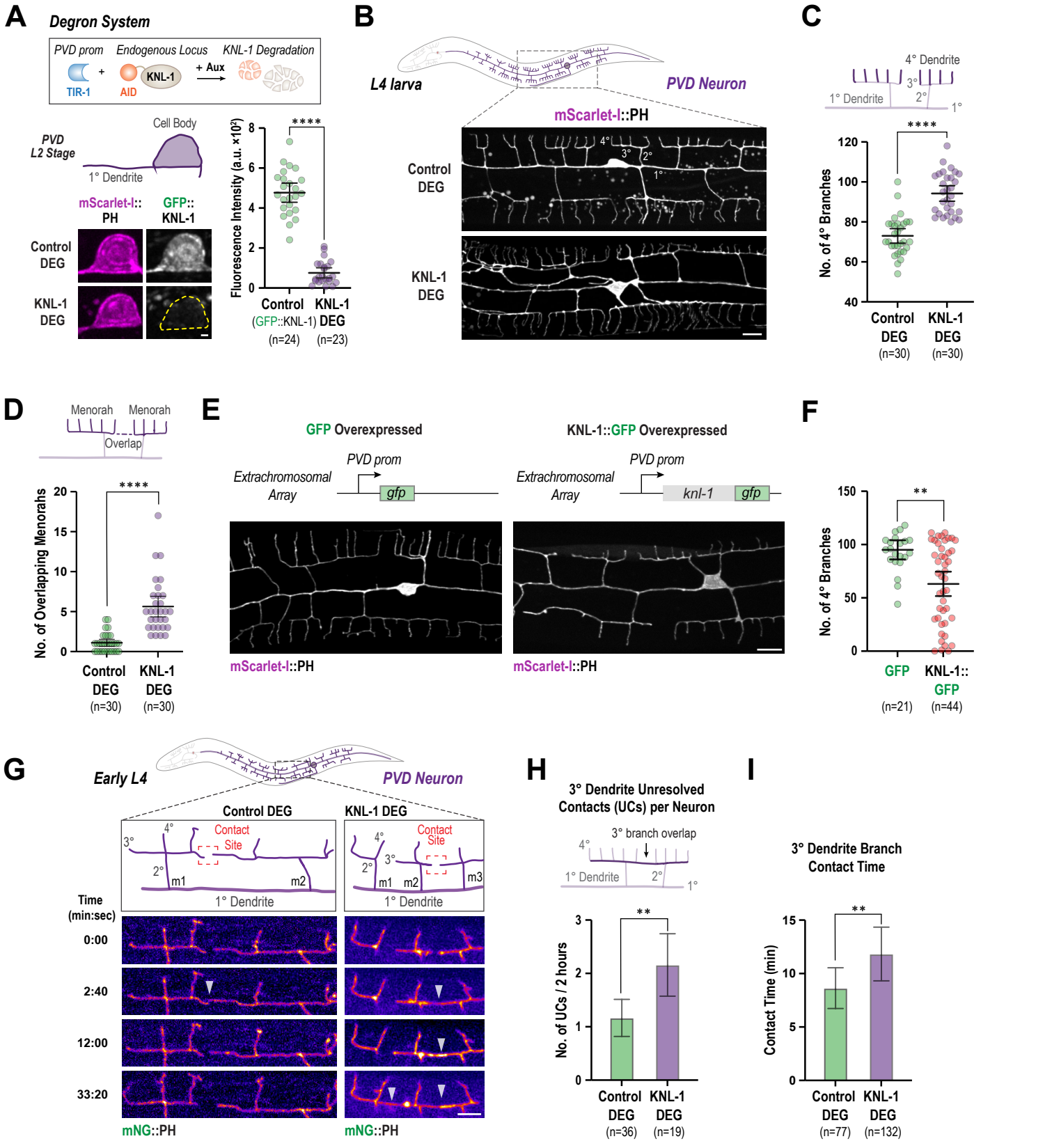

Figure 2: KNL-1 is required for proper dendrite branching of the PVD neuron.

(A) Approach employed for the degradation of endogenously tagged AID::KNL-1 in the PVD neuron (top). Images below show GFP::KNL-1 signal (gray) within the PVD cell body (magenta) at the late L2 larval stage, in the absence (Control DEG) and presence of auxin (KNL-1 DEG). The graph on the right shows the mean fluorescence intensity of the GFP signal in the cell body for control and KNL-1 DEG conditions. n represents number of animals. Error bars indicate mean ± 95% CI. Asterisk **** represent p<0.0001 from unpaired t-test. Scale bar, 1µm. **(B)** Images of PVD dendrite organization at the L4 larval stage in the control and KNL-1 DEG animals. These images show both the anterior and posterior dendrites extending from the cell body within a 100µm region. Scale bar, 10µm. **(C-D)** Quantification of PVD dendrite architecture including number of 4° branches and overlaps between menorahs in control and KNL-1 DEG. n represents number of animals. Error bars represent mean ± 95% CI. Asterisk **** represent p<0.0001 from unpaired t-test (C) or Mann-Whitney test (D). **(E)** Images of PVD dendrites in GFP (control) and KNL-1::GFP overexpressing animals. In both conditions the transgenes were overexpressed as an extrachromosomal array under a PVD specific promoter. n represents number of animals. Scale bars, 10µm. **(F)** Quantification of the number of 4° branches in the PVD in GFP and KNL-1::GFP overexpressing animals. n represents number of animals. Error bars represent mean ± 95% CI. Asterisk ** represent p<0. 01 from Mann-Whitney test. **(G)** Time lapse imaging of 3° dendrite branch dynamics in control and KNL-1 DEG animals. White arrow heads denote the contact sites between 3° dendrites of two adjacent menorahs. Scale bar, 5µm. **(H)** Quantification of unresolved contacts (UCs) between 3° dendrites. n represents number of animals. Error bars represent mean ± 95% CI. Asterisk ** represent p<0. 01 from Mann-Whitney test. **(I)**. Quantification of time spent in contact by 3° dendrites of two adjacent menorahs. n represents number of contacts. Error bars represent mean ± 95% CI. Asterisk ** represent p<0. 01 from Mann-Whitney test.

Figure 3

Green et al.

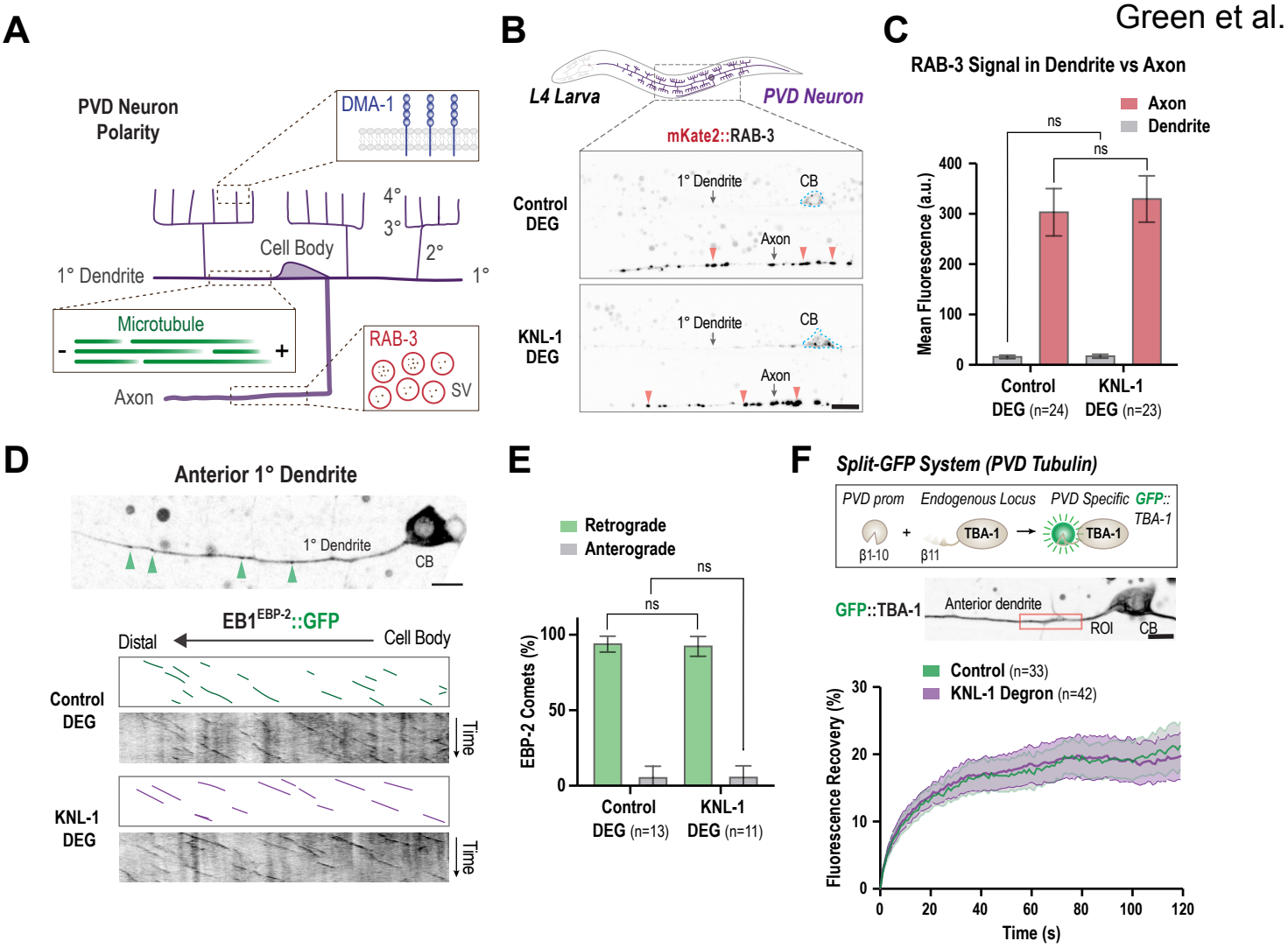

Figure 3: PVD neuronal polarity & microtubule organization are not affected by degradation of KNL-1.

(A) Schematic showing the intracellular organization of the PVD anterior dendrite and axon. DMA-1 is a dendrite specific receptor and RAB-3 is found in the membranes of synaptic vesicles (SV) that accumulate in the axon of PVD. Microtubules in the primary anterior dendrite are organized with minus ends facing the dendrite tip and the plus ends point towards the cell body. **(B)** Localization of the synaptic marker RAB-3 in control and KNL-1 DEG. Orange arrowheads indicate RAB-3 puncta. RAB-3 puncta are predominantly enriched in the axon in both conditions. Scale bar, 5μm. **(C)** Quantification of RAB-3 fluorescent signal in the dendrite and axon of the PVD neuron in the indicated conditions. n represents the number of animals. Error bars represent mean ± 95% CI. Asterisk ns represents p>0.05 from one-way ANOVA test followed by Tukey's test. **(D)** $EB1^{EBP-2}$::GFP dynamics in the anterior primary dendrite. Image of the PVD primary anterior dendrite at the L4 larval stage (top). The green arrowheads indicate $EB1^{EBP-2}$ comets in the dendrite. Below are kymographs of $EB1^{EBP-2}$::GFP along the dendrite in control and KNL-1 DEG animals, created from 60s time projection images. Scale bar, 5μm. **(E)** Quantification of $EB1^{EBP-2}$::GFP comet direction in control and KNL-1 DEG. n represents the number of comets. n represents number of animals. Error bars represent mean ± 95% CI. Asterisk ns represents p>0.05 from two-way ANOVA test followed by Šídák's test. (**F)** Schematic of the split GFP system used to express endogenous GFP::TBA-1 specifically in the PVD (top). The image below represents GFP::TBA-1 in the anterior dendrite and the cell body of the PVD. The red rectangle denotes the region along the primary dendrite where photobleaching was performed. Scale bar 5μm. The graph depicts fluorescence recovery of GFP::TBA-1 in control and KNL-1 DEG. n represents the number of animals. Lines and shaded region represent mean ± 95% CI.

Figure 4
Green et al.

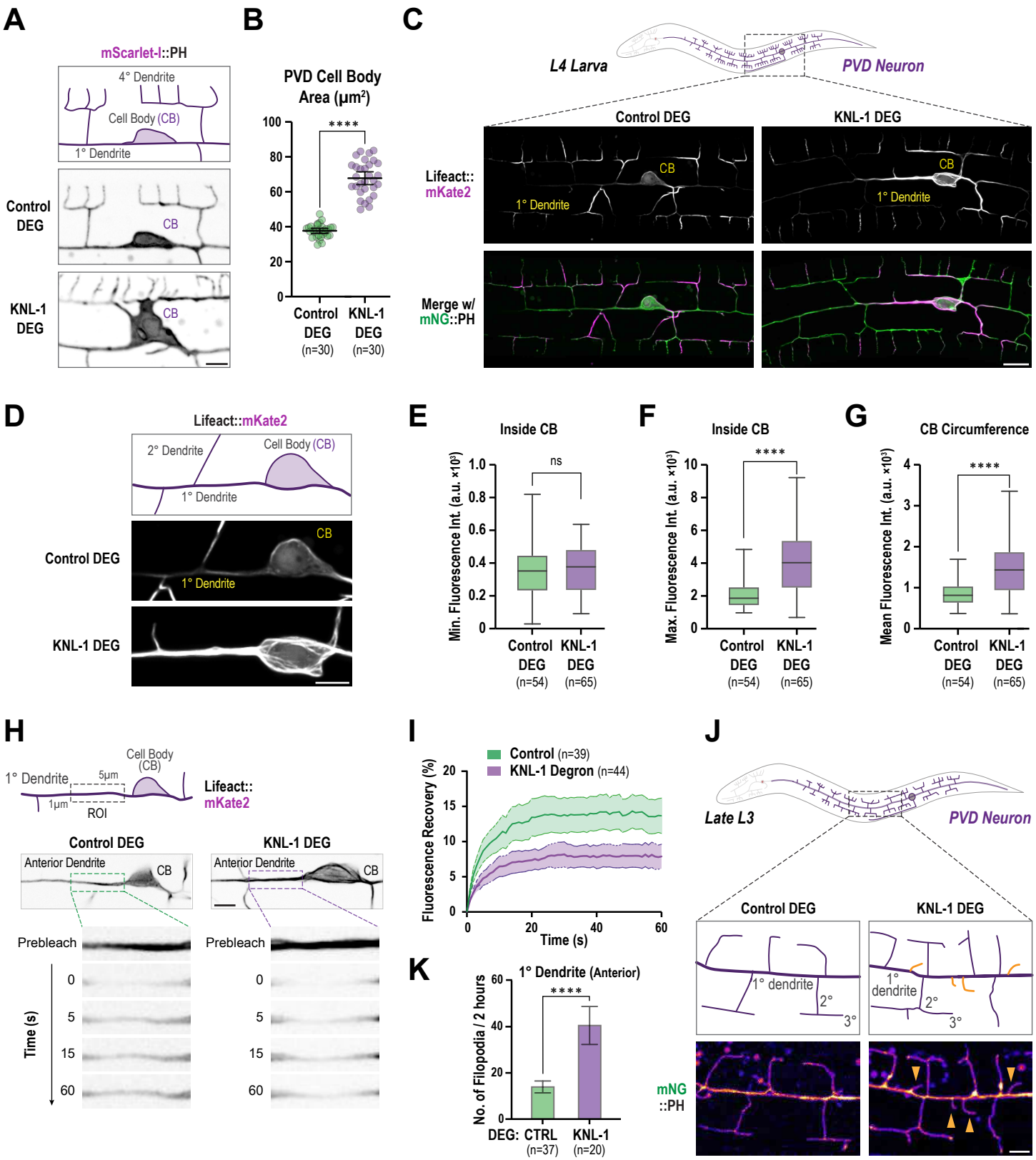

Figure 4: KNL-1 degradation impacts actin dynamics in the PVD neuron.

(A) Images of the PVD cell body (CB) and proximal regions in control and KNL-DEG. Scale bar, 5μm. **(B)** Quantification of the area of the cell body in control and KNL-1 DEG animals. n represents number of animals. Error bars represent mean ± 95% CI. Asterisk **** represents p<0.0001 from Mann-Whitney test. **(C)** Images showing actin distribution (gray in top, magenta in the bottom) in the PVD cell body and dendrites (green). Actin is visualized using Lifeact::mKate2, and the plasma membrane is labelled with mNeonGreen::PH. Scale bar, 10μm. **(D)** Images highlighting actin distribution in the cell body (CB) and proximal anterior primary dendrite in control and KNL-1 DEG animals. Scale bar, 5 μm. **(E&F)** Quantification of minimum and maximum Lifeact::mKate2 fluorescence intensity inside the cell body. n represents the number of animals. Error bars represent minimum and maximum. Asterisk **** represents p<0.0001 from unpaired t-test. (**G)** Quantification of Lifeact::mKate2 fluorescence intensity along a 3-pixel wide line along the circumference of the cell body (CB).n represents the number of animals. Error bars represent minimum and maximum. Asterisk **** represents p<0.0001 from Mann-Whitney test. **(H)** Images of the PVD anterior primary dendrite expressing mKate2::Lifeact in control & KNL-1 DEG animals, at the L4 larval stage. The dashed rectangles denote the region along the primary dendrite where photobleaching was performed. Scale bar, 5 μm The images below represent prebleach and postbleach (0s-60s) frames of mKate2::Lifeact in control and KNL-1 DEG animals. Scale bar, 5μm. **(I)** Graph showing mKate2::Lifeact fluorescence recovery in control and KNL-1 DEG animals. n represents the number of animals. Lines and shaded region represent mean ± 95% CI. **(J)** Images of the anterior primary dendrite labeled with mNeonGreen::PH in control and KNL-1 DEG, in late L3 larval stage animals. Orange arrowheads indicate filopodial protrusions. Scale bar, 5μm. **(K)** Quantification of the filopodial protrusions from anterior primary dendrite over a two-hour

time interval. n represents the number of animals. Error bars represent mean ± 95% CI. Asterisk **** represents $p<0.0001$ from unpaired t-test.

Figure 5

Green et al.

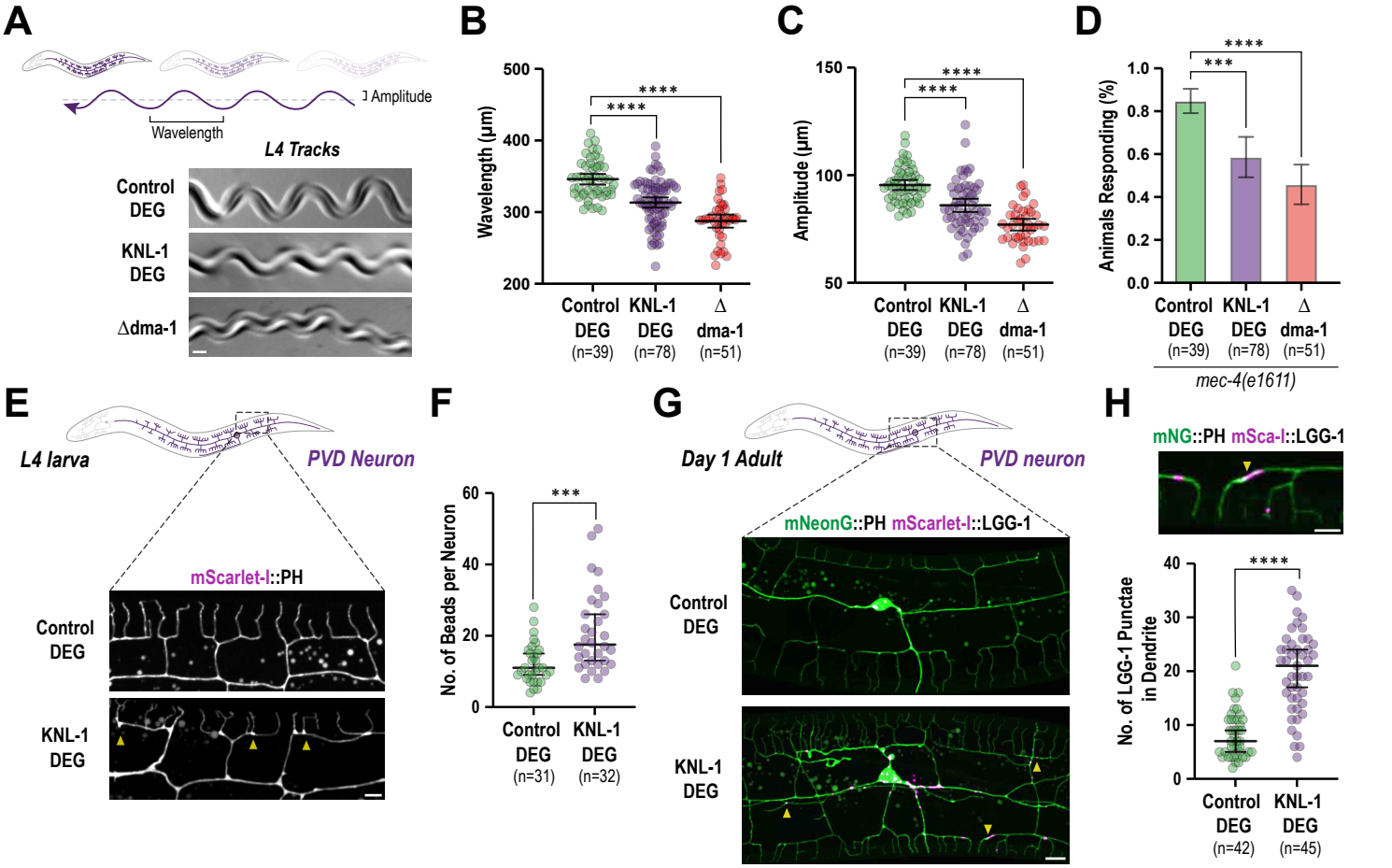

Figure 5: KNL-1 is important for PVD neuron sensory behavior and maintenance.

(A) A visual representation of animal movement is depicted in a cartoon, where the arrow represents the track that animal leaves behind (top). Images show the tracks of control, KNL-1 DEG and Δ*dma-1* animals. The control worms form sinusoidal tracks while the amplitude and wavelength of these tracks were diminished in KNL-1 DEG and Δ*dma-1* animals. Scale bar 20μm **(B-C)** Quantification of the wavelength and amplitude of the tracks by animals in indicated conditions n represents the number of animals. Error bars represent mean ± 95% CI. Asterisk **** represents p<0.0001 from Kruskal-Wallis test followed by Dunn's test (B) or one-way ANOVA test followed by Tukey's test (C). **(D)** The plot represents the number of animals responding to harsh touch in the indicated conditions. The experiment was conducted in *mec-4(e1611)* mutant background, which lacks touch receptor neurons. n represents the number of animals. Error bars represent mean ± 95% CI. Asterisk **** represents p<0.0001 from Kruskal-Wallis test followed by Dunn's test. (**E)** Images of PVD dendrite organization at the L4 stage in control and KNL-1 DEG animals. Yellow arrowheads indicate the bead-like blebs in the plasma membrane of PVD neuron. Scale bar, 5μm. **(F)** Quantification of the bead-like blebs in control and KNL-1 DEG animals. n represents number of animals. Error bars represent mean ± 95% CI. Asterisk *** represents p<0.001 from Mann-Whitney test. (**G)** Images show PVD cell body and dendrites (green) and autophagosomes (magenta) in the indicated conditions. Yellow arrowheads indicate the appearance of LGG-1 puncta along the dendrites of KNL-1 DEG animals. Scale bar 10μm. **(H)** A zoomed image of the PVD dendrite showing the plasma membrane in green and autophagosomes in magenta (top). The plot below is the quantification of mScarlet-I (mSca-I)::LGG-1 puncta within the dendrites in both control and KNL-1 DEG animals. n represents the number of animals. Error bars represent mean ± 95% CI. Asterisk **** represents p<0.0001 from unpaired t-test. Scale bar 5μm.

Figure S1

Green et al.

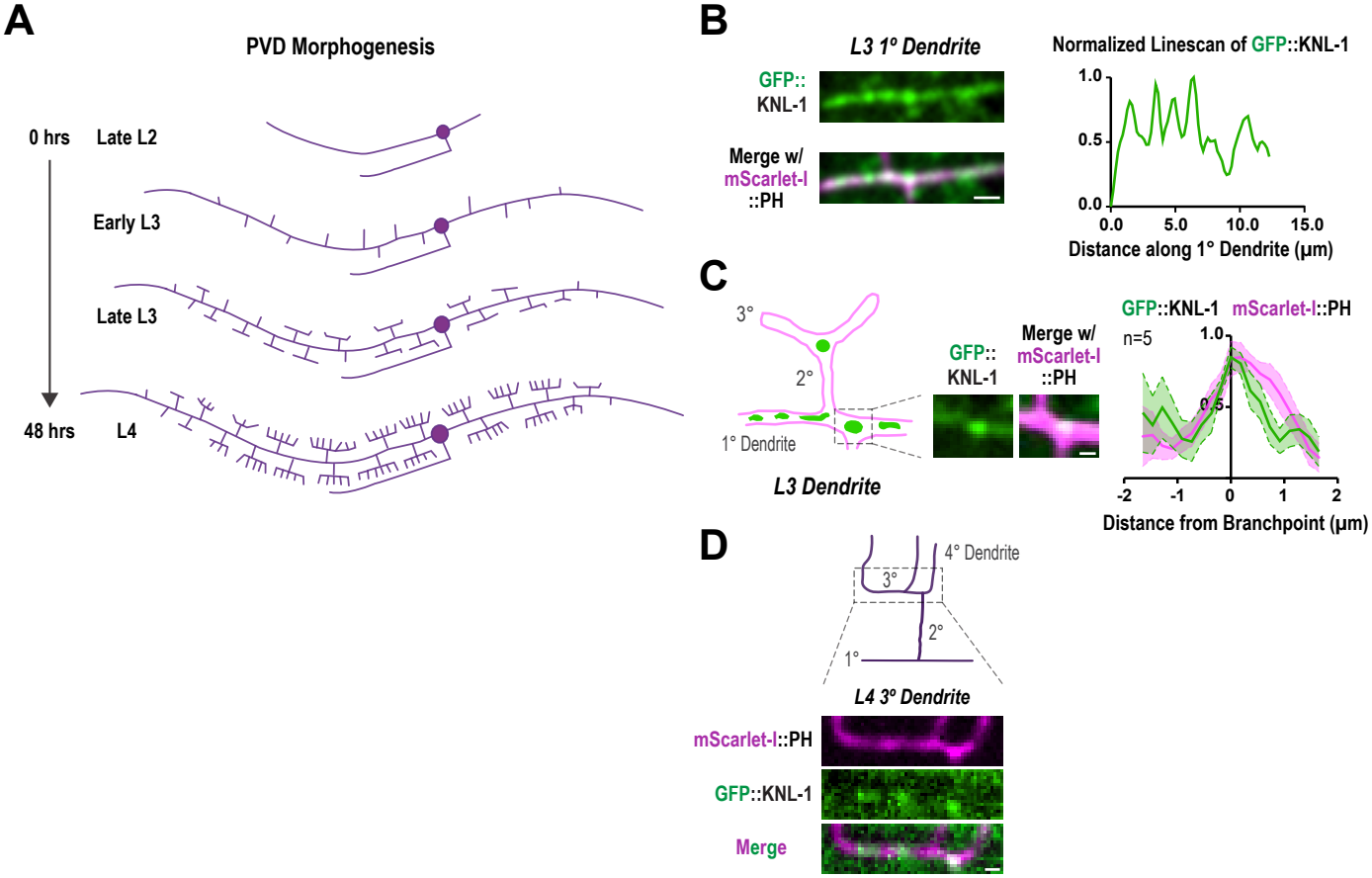

Figure S1. PVD morphogenesis & KNL-1 localization.

(A) Schematic representing the PVD neuron morphogenesis during the larval stages of *C. elegans*. PVD development initiates at the L2 larval stage. By the late L2 stage, the anterior and posterior primary branches, along with the axon begins to extend. The primary (1°) dendrites are fully extended by the early L3 stage and secondary (2°) dendrites begin to emerge. During the late L3 and L4 stages, there is extensive branching as the tertiary (3°) and quaternary (4°) branches start growing. By the late L4 larval stage (approximately 48 hours at 20°C) the "menorah" structures are fully formed. **(B)** Localization of GFP::KNL-1 within the primary (1°) dendrite at the L3 stage. KNL-1 forms distinct puncta-like structures along the 1° dendrite (left). The bottom panel is a merge of the GFP::KNL-1 with the membrane marker mScarlet-I::PH. Scale bar, 2 µm. Linescan of the GFP::KNL-1 fluorescent intensity (right). The peaks correspond to the puncta seen in the image. **(C)** Schematic and image showing GFP::KNL-1 enrichment at the branchpoint between 1° and 2° dendrite at the L3 stage (left). Scale bar, 1 µm. Graph showing linescan of the average fluorescent intensity of GFP::KNL-1 superimposed with that of the membrane marker mScarlet-I::PH. n represents number animals. Dotted lines and shaded region represent mean ± SEM. Branchpoints show an increased intensity of both PH and KNL-1 signal. **(D)** Image shows distribution of GFP::KNL-1 along the 3° dendrite at the early L4 stage. Scale bar, 2 µm.

Figure S2

Green et al.

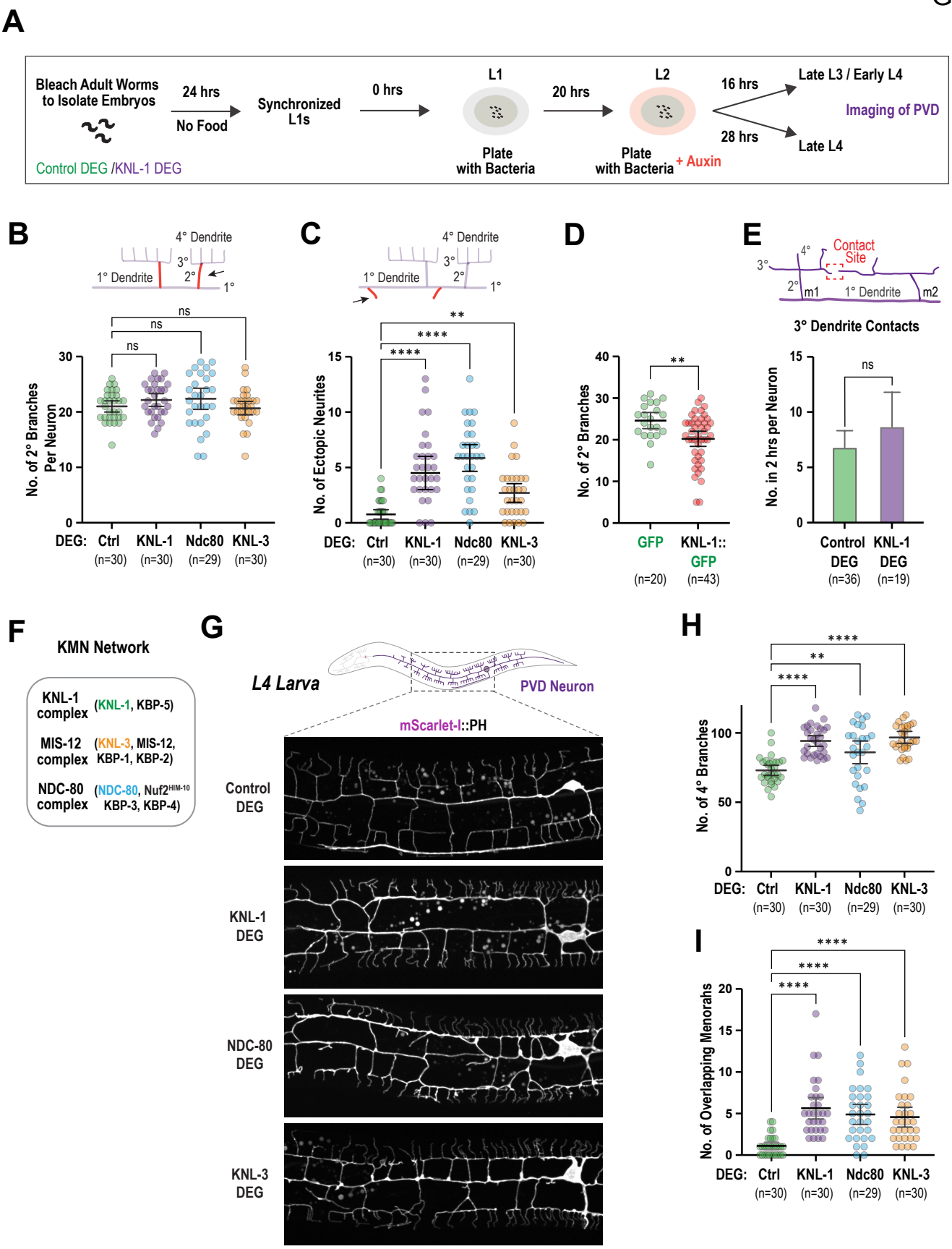

Figure S2. Effects of degradation of KMN network on PVD morphology.

(A) Schematic indicating the experimental design for degrading AID::KNL-1. To obtain synchronized L1 animals, embryos from control or AID::KNL-1 adult worms expressing PVD-specific TIR1 transgene were isolated by treating the worms with bleach and hatched for 24 hours on plates without food. The arrested L1 larvae were placed on a plate with food until they reached the L2 stage (20hrs). The late L2 stage animals were transferred to plates with food and auxin and grown until they reached L3 (16hrs) or L4 stage (24hrs). The late L4 stage animals, which have fully developed menorahs, were imaged to analyze the PVD morphology. **(B-C)** Quantification of the numbers of 2° branches and the number of ectopic branches in the indicated conditions. n represents the number of animals. Error bars represent mean ± 95% CI. Asterisk ns represents $p>0.05$ from Kruskal-Wallis test followed by Dunn's test. **(D)** Quantification of the number of 2° branches in the PVD in GFP and KNL-1::GFP overexpressing animals, n represents the number animals. Error bars represent mean ± 95% CI. Asterisk ** represents $p<0.01$ from Mann-Whitney test. **(E)** Number of contacts made by tertiary dendrites of the PVD neuron over a two hour time interval in the indicated conditions. n represents number of animals. Error bars represent mean ± 95% CI. Asterisk ns represents $p>0.05$ from Mann-Whitney test. **(F)** Schematic of the KMN network complexes (KNL1/Mis12/Ndc80) and their components. **(G)** Images of PVD dendrite organization in control, KNL-1 DEG, NDC-80 DEG & KNL-3 DEG animals. Scale bar, 10 µm. **(H-I)** Quantification of 4° branches and overlaps between menorahs in the indicated conditions. n represents the number of animals. Error bars represent mean ± 95% CI. Asterisk **** represents $p<0.0001$ from Kruskal-Wallis test followed by Dunn's test.

Figure S3. DMA-1 distribution, microtubule organization & filopodia dynamics after degradation of KNL-1 in the PVD.

(A) Localization of the dendrite guidance receptor, DMA-1 in control and KNL-1 DEG at the L4 larval stage. Pink arrow heads show enrichment of DMA-1 in the 4° dendrite. Scale bar, 10μm. DMA-1 is restricted to dendrite structures and no axonal signal for DMA-1 is visible. **(B)** Quantification of DMA-1 fluorescent signal in the PVD 4° dendrites. Both the control and KNL-1 DEG present similar levels of DMA-1. n represents number of animals. Error bars represent mean ± 95% CI. Asterisk ns represents p>0.05 from unpaired t-test. **(C)** Images display expression of GFP::TBA-1 driven by *des-2* promoter in control and KNL-1 DEG animals. Tubulin distribution looks similar in both conditions. GFP::TBA-1 is predominantly localized to the 1° dendrite and is also observed in the 2° and 3° dendrite branches. Scale bar, 10 μm. **(D-E)** Quantification of $EB1^{EBP-2}$::GFP comet dynamics in control and KNL-1 DEG. n represents the number of comets and number of animals respectively. Error bars represent mean ± 95% CI. Asterisk ns represents p>0.05 from Mann-Whitney test (D) or unpaired t-test (E). **(F)** Still images of the PVD anterior primary dendrite expressing endogenous GFP::TBA-1 in control and KNL-1 DEG animals (top). Scale bar, 5 μm. The dashed rectangles indicate regions that were photobleached in the FRAP experiments. Pre-bleach and post-bleach images of GFP::TBA-1 in control and KNL-1 DEG animals. **(G)** Snapshots of time lapse imaging of 1° dendrite branch dynamics in control and KNL-1 DEG animals at the late L3 stage. Yellow arrowheads indicate already established filopodia. White asterisks indicate newly formed filopodia. Yellow asterisks indicate the misguided filopodia that run parallel to the 1° dendrite. Scale bar, 5 μm

Figure S3
Green et al.

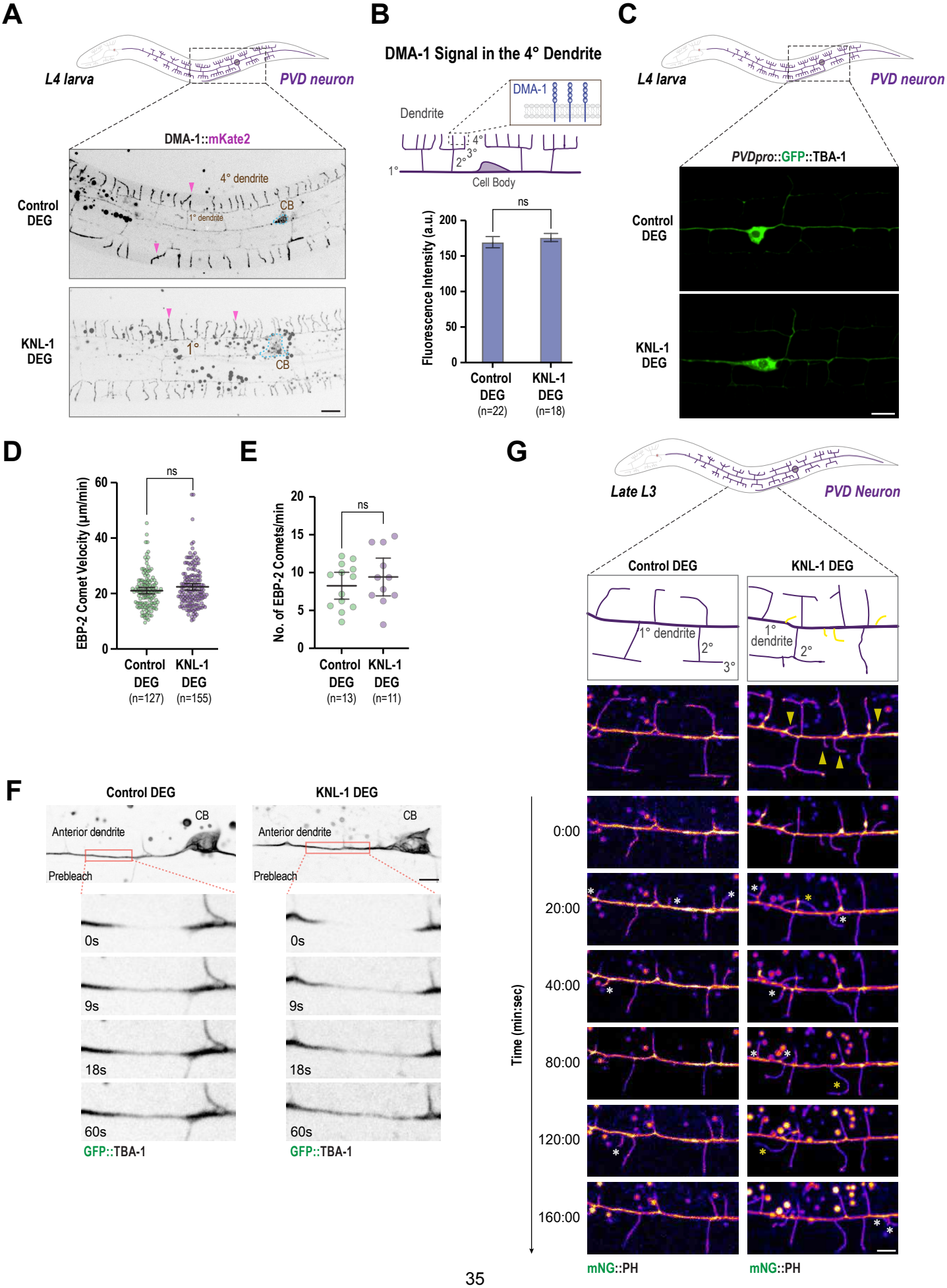

Materials and Methods

C. elegans strains

C. elegans strains were maintained in nematode growth media (NGM) plates seeded with the *Escherichia coli* OP50 strain at 20°C. The genotypes of the *C. elegans* strains used in this study are described in Key Resource Table.

Recombinant plasmid DNA

All plasmids used in this study were made using the Gibson Assembly method (Gibson et al., 2009) and the DNA sequences were confirmed by Sanger sequencing.

Generation of transgenic C. elegans strains

Single copy transgenic integrations were engineered using the transposon based Mos1 mediated Single Copy Insertion (MosSCI) method(Frøkjaer-Jensen et al., 2008). The transgenes were cloned into pCFJ151 for insertion into chromosome I(*oxTi185*), II(*ttTi5605*), IV(*oxTi177*) or V(*oxTi365*) mos1 insertion sites. Information on the promoters used for expression of the transgenes can be found in Table S2. A mix of repair plasmids that contains the transgene of interest, positive selection marker, transposase plasmid and three fluorescent markers for negative selection [pCFJ90 (Pmyo-2::mCherry), pCFJ104 (Pmyo-3::mCherry) and pGH8 (Prab-3::mCherry)] was injected into appropriate *C. elegans* strains that contain the mos1 insertion sites. Transformants were selected based on their ability to rescue the mobility defect of the parental strains and successful integrants were identified by PCR genotyping.

The transgenic strains containing extrachromosomal arrays (*dhaEx1 and dhaEx3)* were generated by injecting plasmid construct mix containing either 50ng/μl pDC1031or pDC1032, 2ng/μl pCFJ90, and 50ng/μl of empty pBluescript SK as carrier DNA into young adult hermaphrodites of the strains DKC410 that expressed the transgene P*des-2::*mScarlet-I::PH::*unc-54*::3'UTR *from oxTi177 mos1 locus on Chr IV.*

CRISPR/Cas9-mediated genome editing

Endogenous tagging of various genes (see Table S2) at the N- or C-terminus and generation of the *dma-1* deletion and *mec-4(e1611)* allele mimic that contains the A713V mutation were done using CRISPR/Cas9 methods(Dickinson et al., 2015; Paix et al., 2015). The specific method, guide RNA sequences and homology arm sequences used to generate each strain are described in Table S3. Briefly, a DNA mix or Cas9RNP mix, containing the respective repair template, guide RNA sequences, Cas9 and selection markers were injected into N2 animals except for *dha185* allele for which DKC1139 strain was used. Recombinant strains were identified by appropriate selection method and by genotyping PCR and the sequences were confirmed using Sanger sequencing of the edited genomic region.

Synchronization protocol for C. elegans to follow PVD Morphogenesis

To track PVD morphogenesis, *C. elegans* animals were synchronized at the L1 arrest stage through the following procedure. Gravid adults were bleached on NGM plates using a solution containing 1M sodium hydroxide and 2.5% sodium hypochlorite to extract eggs. These eggs were then allowed to incubate for 48 hours on NGM plates without food at 20°C, allowing them to develop into L1 larvae and enter the L1 arrest stage. The arrested L1 animals were washed off the plates with M9 buffer, transferred to a centrifuge tube, and pelleted through centrifugation at 1000 RPM for 1 minute. The arrested L1 larvae were then placed onto NGM plates seeded with OP50 bacteria, designated as T=0 hours, and grown at 20°C. Under these conditions, the developmental stages following the transfer on to NGM plate with food corresponded to: L2 (20 hours), late L3 (36 hours), and late L4 (48 hours).

Auxin Degradation

The auxin treatment was conducted by growing animals on NGM plates supplemented with 4mM auxin (K-NAA, N160, Phytochrome Laboratories), following the protocol described in (Ashley et al., 2021). For efficient degradation of AID-tagged proteins, we

expressed TIR1 under two distinct promoters within the PVD neurons: *unc-86*pro and *des-2*pro. To ensure targeted degradation of AID-tagged proteins specifically in PVD neurons after birth, synchronized animals were transferred to NGM plates containing auxin and OP50 *E. coli* at the late L2 stage (20 hours post-synchronization). In all experiments except the time-lapse imaging of PVD dendrite dynamics using mNeonGreen::PH membrane marker, TIR1 transgene expressing animals exposed to auxin were used as control. For time-lapse imaging experiments recording PVD dendrite dynamics, animals expressing both the AID fusion and TIR1 transgenes, but not exposed to auxin, were used as control.

Behavioural assays

To conduct the locomotion assays, L4 stage worms were incubated for one hour at 20°C on a freshly seeded NGM plate prepared the day before. Subsequently, the tracks left by the worms were recorded using a Nikon SMZ18 microscope equipped with a 2X P2-SHR Plan Apo 1X objective and a Photometrics Cool SNAP camera. For each worm, 5 tracks were analysed, and this process was repeated for 15 animals per condition. The measurement of track characteristics included determining the track wavelength, which was defined as the distance between two successive peaks, and the track amplitude, which was calculated as half of the height between two opposing peaks. In total, five measurements were taken for each track to ensure accuracy and consistency in the analysis.

Harsh touch response was assessed by prodding non-moving gravid day 1 adult *C. elegans* animals with a platinum wire to the midsection of the body, following previously established methods (Way and Chalfie, 1989). The animals were prodded using a long and flattened tip of a wire platinum pick either at or just behind the vulva region. Each individual animal was subjected to this prodding test 3 times, with 10 minute intervals between trials. Animals that backed up upon prodding was scored as

sensitive to harsh touch. For each condition, 15 *C. elegans* animals were tested and this process was repeated 4 times. All *C. elegans* animals used for this assay were in the *mec-4(e1611)* mutant mimic background which allowed for the specific isolation of the harsh touch response of the PVD neuron (Chatzigeorgiou et al., 2010). The harsh touch response analysis were carried out blind to genotypes.

Fluorescence microscopy

To image PVD neurons expressing the appropriate markers, L2, L3 or L4 stage worms were anaesthetized in 5mM Levamisole and mounted in M9 on a 2% agarose pad. Images were acquired using a spinning disk confocal imaging system with a Yokogawa spinning disk unit (CSU-W1), a Nikon Ti2-E fully motorized inverted microscope and a Photometrics Prime 95B camera. In most experiments, a CFI60 Plan Apochromat lambda 60X Oil (Nikon) objective was used to image the PVD neurons except when imaging Lifeact::mKate2 marker within the PVD neuron, where a CFI60 Plan Apochromat lambda 100X Oil (Nikon) objective was employed. To visualize the cell body and the dendrite branches at various developmental stages, Z-stacks of either 0.5 µm or 1.0 µm thickness were acquired from the PVD L/R neuron, whichever was closest to the side facing the coverslip / objective.

Time-lapse Imaging

In all experiments involving time-lapse imaging, samples were prepared, and images were acquired as described above. Specifically, for time-lapse imaging of PVD dendrite growth dynamics utilizing the mNeonGreen::PH membrane marker, synchronized L3 stage *C. elegans* animals were anesthetized in 5mM Levamisole and mounted on 2% agarose pads. A region approximately 100 µm from the cell body along the anterior dendrite was chosen for this analysis. Time-lapse sequences were captured, comprising 9-11 z-planes with a spacing of 0.9 µm, at a rate of 1 frame per 20 minutes for 2 hours. Acquisition was performed using a spinning disc confocal imaging system with a

Yokogawa spinning disk unit (CSU-W1), a Nikon Ti2-E fully motorized inverted microscope, with a CFI60 Plan Apochromat lambda 60X Oil (Nikon) objective and Photometrics Prime 95B camera.

To image EB1^{EBP-2}::GFP dynamics, synchronized L4 stage *C. elegans* animals were anaesthetized in 5mM levamisole and mounted in M9 on 2% agarose pads. Movies of a single z-slice within a 50μm region adjacent to the cell body along the anterior dendrite were recorded. The movies were acquired at a rate of 1 frame per 1 sec with a CFI60 Plan Apochromat lambda 100X Oil (Nikon) objective and a spinning disc confocal imaging system as described above.

Fluorescence Recovery After Photobleaching (FRAP) experiments

For the FRAP experiments involving GFP::TBA-1 and Lifeact::mKate2, *C. elegans* animals were anesthetized in 5mM Levamisole and mounted in M9 on 2% agarose pads. The FRAP was performed along the primary dendrite within a region adjacent to the cell body. Before photobleaching, a single z-slice of the anterior dendrite, 50μm from the cell body was acquired at 1 frame per 1 sec using a spinning disc confocal imaging system with a Yokogawa spinning disk unit (CSU-W1), a Nikon Ti2-E fully motorized inverted microscope, with a CFI60 Plan Apochromat lambda 100X Oil (Nikon) objective and Photometrics Prime 95B camera. Following the acquisition of 3 prebleach frames, a 1.5μm region, positioned 20μm away from the cell body was subjected to photobleaching using a 405 nm laser. The fluorescence recovery after photobleaching was recorded at a rate of 1 frame per 1 sec for a duration of 2 minutes.

Image analysis

All image analysis was performed using Image J (Fiji). In summary, the Z-stacks were transformed into a maximum intensity projection (MIP), and the subsequent analysis was conducted on these MIPs to obtain the specified measurements as detailed below, unless

stated otherwise. All the measurements were plotted using GraphPad Prism (GraphPad Software).

Fluorescence intensity profile GFP::KNL-1 along the dendrite

To visualize the distribution of GFP::KNL-1 along the dendrite, a 1-pixel-wide segmented line was drawn along the primary anterior dendrite, using Image J (Fiji). For quantifying the co-localization of mScarlet-I::PH with GFP::KNL-1 at PVD branchpoints, a 1-pixel-wide segmented line was traced along the anterior dendrite of PVD, 2 µm on either side of the branchpoint or base of the branch. The maximum and minimum fluorescence intensity profiles along the segmented lines were recorded using Fiji's "Plot Profile" function for all wavelengths. The values were then normalized to the maximum and minimum intensity values, ($\frac{x-minimum}{maximum-minimum}$).

Quantification of GFP::KNL-1 degradation

To quantify KNL-1 degradation within the cell body of the PVD neurons expressing GFP::KNL-1 and GFP::KNL-1::AID, the region corresponding to the cell body was defined by employing a polygon selection tool in Image J(Fiji) to outline the cell body boundary in mScalet-I::PH marker. The mean intensity of GFP::KNL-1::AID within the cell body was measured and normalized to background mean intensity of a comparable region outside of the neuron.

Quantification of PVD dendrite morphology parameters

Various parameters related to dendrite morphology were individually assessed for both posterior dendrite and the proximal anterior dendrite, located 100µm from the soma, in *C. elegans* animals expressing the mNeonGreen::PH membrane marker. The secondary (2°) dendrites were identified as branches orthogonal to the primary (1°) dendrite that exhibited higher order branching, including tertiary (3°) and/or quaternary (4°) branches. The 4° dendrites were recognized as orthogonal branches to the 3^odendrites. Overlapping menorahs were characterized as two adjacent 3° dendrites lacking a gap as described

previously (Smith et al., 2012). Ectopic branches were defined as structures extending from the 1° dendrite with a length of at least twice their width and devoid of higher order branches. To determine the cell body area, a region was defined along the perimeter of the cell body using the polygon selection tool in Image J (Fiji), and the area under the selected region was then quantified. While quantifying PVD dendrite morphology parameters for strains with extrachromosomal arrays expressing GFP and KNL1::GFP, only animals with normalized GFP intensity values within the cell body that exceeded half of the maximum recorded intensity were considered for analysis. To establish this threshold, we initially measured the maximum fluorescent intensities of GFP or KNL-1::GFP within the region demarcated by a polygon selection outlining the cell body boundary in Image J (Fiji). Subsequently, the fluorescent intensity values were standardized by normalizing them against the background fluorescence intensity of a similar region outside the neuron.

Quantification of PVD dendrite dynamics

The duration of contact between 3° dendrites, number of contacts and number of unresolved of contacts were quantified by analysing maximum intensity projections of Z-stacks obtained from the time-lapse movies using Image J(Fiji). These measurements were carried out within a 100μm region along the PVD neuron, positioned anterior to the cell body. Contacts between 3° dendrites were defined as instances where two adjacent 3° dendrites in direct contact without any visible gap, following the criterion described previously (Smith et al., 2010). Only the contacts that occurred during the time-lapse acquisition were included in the quantification. Unresolved contacts (UCs) were defined as contacts between 3° dendrites that remained without a gap by the end of the time-lapse. Additionally, for Figure 5K, filopodial protrusions were defined as any membrane extensions originating from the primary dendrite that were smaller than 2.5 μm in length.

Analysis of membrane blebbing

To quantify membrane blebbing, we examined the entire anterior dendrite by analysing maximum intensity projections of *C. elegans* animals expressing the mScarlet-I::PH membrane marker at the L4 stage. Bead-like structures observed on the membrane were categorized as "blebbing events" based on an analysis of dendrite width. Specifically, we measured the dendrite width, compared any variations in width, and used an empirically determined threshold of 1.5 times the width of the flanking membrane as a criterion for defining beads or blebbing events.

Counting of mScarlet-I::LGG-1 puncta

mScarlet-I::LGG-1 was found in the dendrites, axon initial segment, and cell body, but for our analysis, we only considered the mScarlet-I::LGG-1 puncta along the dendrites. To quantify the number of mScarlet-I::LGG-1 puncta, we applied a threshold arbitrarily (set at >10X the local diffuse background signal) to the fluorescence intensity profile plot along the dendrites of day 3 adult animals.

Analysis of mKate2::RAB-3 and DMA-1::mKate2 fluorescent intensity

mKate2::RAB-3 is primarily concentrated in the axon of the PVD neuron; however, the mKate2 signal was present throughout the neuron, effectively outlining the morphology of the PVD neuron. To evaluate the distribution of mKate2::RAB-3, we quantified the mean fluorescence intensity of mKate2::RAB-3 puncta along both the length of the axon of each neuron and a corresponding length in the proximal anterior dendrite. To do this, we initially drew a segmented line with a width of 3 pixels along the axon and a matching line with similar width and length along the primary dendrite. Subsequently, we recorded the mean fluorescence intensity along these segmented lines using Image J (Fiji). To account for background fluorescence, a parallel segmented line was traced outside the neuron to obtain a background intensity measurement, and this value was then subtracted from the mean fluorescence intensity to normalize the results.

For DMA-1::mKate2, which is enriched in the quaternary dendrites, we quantified the mean fluorescence intensity of the puncta along the 4° dendrites adjacent to the cell body. Notably, the mKate2 signal in DMA-1::mKate2-expressing animals was observed within the dendrites and cell body, while being absent from the axons. The measurement process for DMA-1::mKate2 fluorescence intensity along the dendrites closely mirrored that of mKate2::RAB-3. Specifically, a 3-pixel wide segmented line was traced along the 4° dendrites, and the mean fluorescence intensity was calculated. The measured fluorescence intensity values were normalized by subtracting the background fluorescence, measured along a corresponding segmented line outside the neuron.

FRAP analysis

To measure fluorescence intensity after photobleaching for GFP::TBA-1 and Lifeact::mKate2, a region of interest (ROI) with a diameter of 1.5 µm was chosen using the elliptical selection tool in Image J (Fiji). At each time point, we measured the fluorescence intensity within this elliptical region and then adjusted it by subtracting the background fluorescence intensity obtained from a comparably sized region located outside the neuron. Additionally, to account for bleaching during image acquisition, we performed a correction by dividing the value of the bleached area by the value of the unbleached area, compensating for this loss.

Quantification of actin in the PVD neuron

To evaluate the distribution of actin around and within the PVD neuron cell body, Lifeact::mKate2 Z-stacks composed of approximately 18 x 1 µm Z-planes were projected as a maximum intensity projection. To determine the circumference of the cell body, a segmented line of 3 pixels width was drawn around the cell body, starting at the anterior side, and tracing along the cell body boundary in a clockwise direction using Image J (Fiji). A corresponding line of the same width was placed outside the neuron to calculate the

background fluorescence intensity. The mean Lifeact::mKate2 fluorescence intensity along the cell body circumference was measured and normalized to the background.

To assess the distribution of actin filaments within the cell body, the region corresponding to the cell body was outlined using a polygon selection tool in Image J (Fiji). Within this defined area, the standard deviation, maximum, and minimum intensity of Lifeact::mKate2 were determined. A similar polygonal region outside the neuron served to measure the background fluorescence intensity and normalize the measured Lifeact::mKate2 intensity values within the cell body.

Quantification and Statistical Analysis

Details of the methods employed to extract and quantify various parameters in microscopy datasets are described in the image analysis section. The statistical tests used to determine significance are described in the figure legends. The data normality was assessed using a Shapiro-Wilk test. For normally distributed data either an unpaired t-test (for comparisons between two groups), an ordinary one-way ANOVA with a follow up Tukey's multiple comparison test (for comparisons between three and more groups) or a two-way ANOVA with a follow up Šídák's multiple comparison test (for comparisons with two or more independent variables) were performed. For data sets that did not pass the normality test either a Mann-Whitney test (for comparisons between two groups) or a Kruskal-Wallis test with a follow up Dunn's multiple comparison test (for comparisons between three and more groups) were performed. All comparisons were done in GraphPad Prism (GraphPad Software) and the stars ****, ***, ** and ns correspond $p<0.0001$, $p<0.001$, $p<0.01$ and "not significant", respectively.

Supplementary Files

Fig. S1 shows results related to Fig. 1 (description of GFP::KNL-1 localization during L3 stages). Fig. S2 shows results related to Fig. 2 (effect of degradation of Ndc80 complex

and Mis12 complex components on PVD architecture). Fig. S3 shows results related to Fig. 3 (DMA-1 localization and microtubule organization) and Fig. 4 (filopodia dynamics). Table S1 lists C. elegans genotypes. Table S2 lists promoter sequences used for transgene expression. Table S3 lists sequences targeted by CRISPR/Cas9.

ACKNOWLEDGMENTS

We thank Reto Gassmann, Bill Earnshaw, Esther Zanin and Rebecca Green for their valuable feedback on the manuscript. We thank Frank McNally and Martin Harterink for sharing *C. elegans* strains, Ana Carvalho for the Lifeact::mKate2 plasmid, and Dave Kelly and Toni McHugh (Wellcome Centre Optical Instrumentation Laboratory, (COIL)) for microscopy support. Some strains were provided by the CGC, which is funded by NIH Office of Research Infrastructure Programs (P40 OD010440). This work was supported by a Sir Henry Dale Fellowship to D.K.C. jointly funded by the Wellcome Trust and the Royal Society (208833/Z/17/Z), a Sir Henry Wellcome Postdoctoral Fellowship (215925) awarded to B.P. and Darwin Trust PhD Studentships, Edinburgh awarded to H.A.D and V.R.O. Imaging was performed in Centre Optical Instrumentation Laboratory (COIL), which is supported by a Core Grant from the (203149) to the Wellcome Centre for Cell Biology at the University of Edinburgh.

AUTHOR CONTRIBUTIONS

Conceptualization, D.K.C. and M.G. ; Methodology, D.K.C. M.G., H.A.D., V.R.O, and B.P., ; Investigation, M.G., H.A.D., V.R.O, and B.P.; Visualization, D.K.C., M.G., H.A.D., and B.P.; Writing – Original Draft, D.K.C., H.A.D., and B.P.; Funding Acquisition, D.K.C., H.A.D., V.R.O, and B.P.; Resources, C.F., B.P., H.A.D., and M.G.; Supervision, D.K.C.

REFERENCES

Albeg, A., C.J. Smith, M. Chatzigeorgiou, D.G. Feitelson, D.H. Hall, W.R. Schafer, D.M. Miller 3rd, and M. Treinin. 2011. C. elegans multi-dendritic sensory neurons: morphology and function. *Mol. Cell. Neurosci.* 46:308–317.

Ashley, G.E., T. Duong, M.T. Levenson, M.A.Q. Martinez, L.C. Johnson, J.D. Hibshman, H.N. Saeger, N.J. Palmisano, R. Doonan, R. Martinez-Mendez, B.R. Davidson, W. Zhang, J.M. Ragle, T.N. Medwig-Kinney, S.S. Sirota, B. Goldstein, D.Q. Matus, D.J. Dickinson, D.J. Reiner, and J.D. Ward. 2021. An expanded auxin-inducible degron toolkit for Caenorhabditis elegans. *Genetics*. 217. doi:10.1093/genetics/iyab006.

Cao, Y., J. Lipka, R. Stucchi, M. Burute, X. Pan, S. Portegies, R. Tas, J. Willems, L. Will, H. MacGillavry, M. Altelaar, L.C. Kapitein, M. Harterink, and C.C. Hoogenraad. 2020. Microtubule Minus-End Binding Protein CAMSAP2 and Kinesin-14 Motor KIFC3 Control Dendritic Microtubule Organization. *Curr. Biol.* 30:899-908.e6.

Chatzigeorgiou, M., S. Yoo, J.D. Watson, W.-H. Lee, W.C. Spencer, K.S. Kindt, S.W. Hwang, D.M. Miller 3rd, M. Treinin, M. Driscoll, and W.R. Schafer. 2010. Specific roles for DEG/ENaC and TRP channels in touch and thermosensation in C. elegans nociceptors. *Nat. Neurosci.* 13:861–868.

Cheerambathur, D.K., B. Prevo, T.-L. Chow, N. Hattersley, S. Wang, Z. Zhao, T. Kim, A. Gerson-Gurwitz, K. Oegema, R. Green, and A. Desai. 2019. The Kinetochore-Microtubule Coupling Machinery Is Repurposed in Sensory Nervous System Morphogenesis. *Dev. Cell*. 48:864-872.e7.

Cheng, L., J. Zhang, S. Ahmad, L. Rozier, H. Yu, H. Deng, and Y. Mao. 2011. Aurora B regulates formin mDia3 in achieving metaphase chromosome alignment. *Dev. Cell*. 20:342–352.

Demarco, R.S., E.C. Struckhoff, and E.A. Lundquist. 2012. The Rac GTP exchange factor TIAM-1 acts with CDC-42 and the guidance receptor UNC-40/DCC in neuronal protrusion and axon guidance. *PLoS Genet.* 8:e1002665.

Dickinson, D.J., A.M. Pani, J.K. Heppert, C.D. Higgins, and B. Goldstein. 2015. Streamlined Genome Engineering with a Self-Excising Drug Selection Cassette. *Genetics*. 200:1035–1049.

E, L., T. Zhou, S. Koh, M. Chuang, R. Sharma, N. Pujol, A.D. Chisholm, C. Eroglu, H. Matsunami, and D. Yan. 2018. An Antimicrobial Peptide and Its Neuronal Receptor Regulate Dendrite Degeneration in Aging and Infection. *Neuron*. 97:125-138.e5.

Emoto, K., R. Wong, E. Huang, and C. Hoogenraad. 2016. Dendrites: Development and Disease. Springer. 608 pp.

Frøkjaer-Jensen, C., M.W. Davis, C.E. Hopkins, B.J. Newman, J.M. Thummel, S.-P. Olesen, M. Grunnet, and E.M. Jorgensen. 2008. Single-copy insertion of transgenes in Caenorhabditis elegans. *Nat. Genet.* 40:1375–1383.

Halevi, S., J. McKay, M. Palfreyman, L. Yassin, M. Eshel, E. Jorgensen, and M. Treinin. 2002. The C. elegans ric-3 gene is required for maturation of nicotinic acetylcholine receptors. *EMBO J.* 21:1012–1020.

Harasimov, K., J. Uraji, E.U. Mönnich, Z. Holubcová, K. Elder, M. Blayney, and M. Schuh. 2023. Actin-driven chromosome clustering facilitates fast and complete chromosome capture in mammalian oocytes. *Nat. Cell Biol.* doi:10.1038/s41556-022-01082-9.

Harterink, M., S.L. Edwards, B. de Haan, K.W. Yau, S. van den Heuvel, L.C. Kapitein, K.G. Miller, and C.C. Hoogenraad. 2018. Local microtubule organization promotes cargo transport in C. elegans dendrites. *J. Cell Sci.* 131:jcs223107.

He, L., L. van Beem, B. Snel, C.C. Hoogenraad, and M. Harterink. 2022. PTRN-1 (CAMSAP) and NOCA-2 (NINEIN) are required for microtubule polarity in Caenorhabditis elegans dendrites. *PLoS Biol.* 20:e3001855.

He, L., R. Kooistra, R. Das, E. Oudejans, E. van Leen, J. Ziegler, S. Portegies, B. de Haan, A. van Regteren Altena, R. Stucchi, A.M. Altelaar, S. Wieser, M. Krieg, C.C. Hoogenraad, and M. Harterink. 2020. Cortical anchoring of the microtubule cytoskeleton is essential for neuron polarity. *Elife*. 9. doi:10.7554/eLife.55111.

Hertzler, J.I., S.I. Simonovitch, R.M. Albertson, A.T. Weiner, D.M.R. Nye, and M.M. Rolls. 2020. Kinetochore proteins suppress neuronal microtubule dynamics and promote dendrite regeneration. *Mol. Biol. Cell*. 31:2125–2138.

Hu, X., C. Viesselmann, S. Nam, E. Merriam, and E.W. Dent. 2008. Activity-dependent dynamic microtubule invasion of dendritic spines. *J. Neurosci.* 28:13094–13105.

Jan, Y.N., and L.Y. Jan. 2001. Dendrites. *Genes Dev.* 15:2627–2641.

Jan, Y.N., and L.Y. Jan. 2010. Branching out: mechanisms of dendritic arborization. *Nat. Rev. Neurosci.* 11:316–328.

Jaworski, J., L.C. Kapitein, S.M. Gouveia, B.R. Dortland, P.S. Wulf, I. Grigoriev, P. Camera, S.A. Spangler, P. Di Stefano, J. Demmers, H. Krugers, P. Defilippi, A. Akhmanova, and C.C. Hoogenraad. 2009. Dynamic microtubules regulate dendritic spine morphology and synaptic plasticity. *Neuron*. 61:85–100.

Kahn, O.I., P. Schätzle, D. van de Willige, R.P. Tas, F.W. Lindhout, S. Portegies, L.C. Kapitein, and C.C. Hoogenraad. 2018. APC2 controls dendrite development by promoting microtubule dynamics. *Nat. Commun.* 9:2773.

Kamiyama, D., S. Sekine, B. Barsi-Rhyne, J. Hu, B. Chen, L.A. Gilbert, H. Ishikawa, M.D. Leonetti, W.F. Marshall, J.S. Weissman, and B. Huang. 2016. Versatile protein tagging in cells with split fluorescent protein. *Nat. Commun.* 7:929.

Lagana, A., J.F. Dorn, V. De Rop, A.-M. Ladouceur, A.S. Maddox, and P.S. Maddox. 2010. A small GTPase molecular switch regulates epigenetic centromere maintenance by stabilizing newly incorporated CENP-A. *Nat. Cell Biol.* 12:1186–1193.

Leeuwen, F.N., H.E. Kain, R.A. Kammen, F. Michiels, O.W. Kranenburg, and J.G. Collard. 1997. The guanine nucleotide exchange factor Tiam1 affects neuronal morphology; opposing roles for the small GTPases Rac and Rho. *J. Cell Biol.* 139:797–807.

Lefebvre, J.L. 2021. Molecular mechanisms that mediate dendrite morphogenesis. *Curr. Top. Dev. Biol.* 142:233–282.

Lefebvre, J.L., J.R. Sanes, and J.N. Kay. 2015. Development of dendritic form and function. *Annu. Rev. Cell Dev. Biol.* 31:741–777.

Li, Z., L. Van Aelst, and H.T. Cline. 2000. Rho GTPases regulate distinct aspects of dendritic arbor growth in Xenopus central neurons in vivo. *Nat. Neurosci.* 3:217–225.

Liao, C.-P., H. Li, H.-H. Lee, C.-T. Chien, and C.-L. Pan. 2018. Cell-Autonomous Regulation of Dendrite Self-Avoidance by the Wnt Secretory Factor MIG-14/Wntless. *Neuron*. 98:320-334.e6.

Liu, O.W., and K. Shen. 2011. The transmembrane LRR protein DMA-1 promotes dendrite branching and growth in C. elegans. *Nat. Neurosci.* 15:57–63.

Luo, L., T.K. Hensch, L. Ackerman, S. Barbel, L.Y. Jan, and Y.N. Jan. 1996. Differential effects of the Rac GTPase on Purkinje cell axons and dendritic trunks and spines. *Nature*. 379:837–840.

Maniar, T.A., M. Kaplan, G.J. Wang, K. Shen, L. Wei, J.E. Shaw, S.P. Koushika, and C.I. Bargmann. 2012. UNC-33 (CRMP) and ankyrin organize microtubules and localize kinesin to polarize axon-dendrite sorting. *Nat. Neurosci.* 15:48–56.

Merriam, E.B., D.C. Lumbard, C. Viesselmann, J. Ballweg, M. Stevenson, L. Pietila, X. Hu, and E.W. Dent. 2011. Dynamic microtubules promote synaptic NMDA receptor-dependent spine enlargement. *PLoS One*. 6:e27688.

Mogessie, B., and M. Schuh. 2017. Actin protects mammalian eggs against chromosome segregation errors. *Science*. 357. doi:10.1126/science.aal1647.

Musacchio, A., and A. Desai. 2017. A Molecular View of Kinetochore Assembly and Function. *Biology* . 6:5.

Nakayama, A.Y., M.B. Harms, and L. Luo. 2000. Small GTPases Rac and Rho in the maintenance of dendritic spines and branches in hippocampal pyramidal neurons. *J. Neurosci.* 20:5329–5338.

Nguyen, M.M., C.J. McCracken, E.S. Milner, D.J. Goetschius, A.T. Weiner, M.K. Long, N.L. Michael, S. Munro, and M.M. Rolls. 2014. Γ-tubulin controls neuronal microtubule polarity independently of Golgi outposts. *Mol. Biol. Cell*. 25:2039–2050.

Oren-Suissa, M., D.H. Hall, M. Treinin, G. Shemer, and B. Podbilewicz. 2010. The fusogen EFF-1 controls sculpting of mechanosensory dendrites. *Science*. 328:1285–1288.

Ouzounidis, V.R., B. Prevo, and D.K. Cheerambathur. 2023. Sculpting the dendritic landscape: Actin, microtubules, and the art of arborization. *Curr. Opin. Cell Biol.* 84:102214.

Paix, A., A. Folkmann, D. Rasoloson, and G. Seydoux. 2015. High Efficiency, Homology-Directed Genome Editing in Caenorhabditis elegans Using CRISPR-Cas9 Ribonucleoprotein Complexes. *Genetics*. 201:47–54.

Pan, C.-L., C.-Y. Peng, C.-H. Chen, and S. McIntire. 2011. Genetic analysis of age-dependent defects of the Caenorhabditis elegans touch receptor neurons. *Proc. Natl. Acad. Sci. U. S. A.* 108:9274–9279.

Riedl, J., A.H. Crevenna, K. Kessenbrock, J.H. Yu, D. Neukirchen, M. Bista, F. Bradke, D. Jenne, T.A. Holak, Z. Werb, M. Sixt, and R. Wedlich-Soldner. 2008. Lifeact: a versatile marker to visualize F-actin. *Nat. Methods*. 5:605–607.

Scott, E.K., and L. Luo. 2001. How do dendrites take their shape? *Nat. Neurosci.* 4:359–365.

Seetharaman, S., and S. Etienne-Manneville. 2019. Microtubules at focal adhesions - a double-edged sword. *J. Cell Sci.* 132. doi:10.1242/jcs.232843.

Shi, R., D.A. Kramer, B. Chen, and K. Shen. 2021. A two-step actin polymerization mechanism drives dendrite branching. *Neural Dev.* 16:3.

Smith, C.J., J. Watson, W.C. Spencer, T. O'Brien, B. Cha, A. Albeg, M. Treinin, and D.M. Miller III. 2010. Time-lapse imaging and cell-specific expression profiling reveal dynamic branching and molecular determinants of a multi-dendritic nociceptor in C. elegans. *Dev. Biol.* 345:18–33.

Smith, C.J., J. Watson, M.K. VanHoven, D.A. Colón-Ramos, and D.M. Miller. 2012. Netrin (UNC-6) mediates dendritic self-avoidance. *Nat. Neurosci.* 15:731–737.

Sundararajan, L., C.J. Smith, J.D. Watson, B.A. Millis, M.J. Tyska, and D.M. Miller 3rd. 2019a. Actin assembly and non-muscle myosin activity drive dendrite retraction in an UNC-6/Netrin dependent self-avoidance response. *PLoS Genet.* 15:e1008228.

Sundararajan, L., J. Stern, and D.M. Miller 3rd. 2019b. Mechanisms that regulate morphogenesis of a highly branched neuron in C. elegans. *Dev. Biol.* 451:53–67.

Tang, L.T., C.A. Diaz-Balzac, M. Rahman, N.J. Ramirez-Suarez, Y. Salzberg, M.I. Lázaro-Peña, and H.E. Bülow. 2019. TIAM-1/GEF can shape somatosensory dendrites independently of its GEF activity by regulating F-actin localization. *Elife*. 8. doi:10.7554/eLife.38949.

Tao, L., D. Porto, Z. Li, S. Fechner, S.A. Lee, M.B. Goodman, X.Z.S. Xu, H. Lu, and K. Shen. 2019. Parallel Processing of Two Mechanosensory Modalities by a Single Neuron in C. elegans. *Dev. Cell*. 51:617-631.e3.

Taylor, C.A., J. Yan, A.S. Howell, X. Dong, and K. Shen. 2015. RAB-10 Regulates Dendritic Branching by Balancing Dendritic Transport. *PLoS Genet.* 11:e1005695.

Threadgill, R., K. Bobb, and A. Ghosh. 1997. Regulation of dendritic growth and remodeling by Rho, Rac, and Cdc42. *Neuron*. 19:625–634.

Tsalik, E.L., T. Niacaris, A.S. Wenick, K. Pau, L. Avery, and O. Hobert. 2003. LIM homeobox gene-dependent expression of biogenic amine receptors in restricted regions of the C. elegans nervous system. *Dev. Biol.* 263:81–102.

Way, J.C., and M. Chalfie. 1989. The mec-3 gene of Caenorhabditis elegans requires its own product for maintained expression and is expressed in three neuronal cell types. *Genes Dev.* 3:1823–1833.

Yan, J., D.L. Chao, S. Toba, K. Koyasako, T. Yasunaga, S. Hirotsune, and K. Shen. 2013. Kinesin-1 regulates dendrite microtubule polarity in Caenorhabditis elegans. *Elife*. 2:153.

Yasuda, S., F. Oceguera-Yanez, T. Kato, M. Okamoto, S. Yonemura, Y. Terada, T. Ishizaki, and S. Narumiya. 2004. Cdc42 and mDia3 regulate microtubule attachment to kinetochores. *Nature*. 428:767–771.

Zhao, G., A. Oztan, Y. Ye, and T.L. Schwarz. 2019. Kinetochore Proteins Have a Post-Mitotic Function in Neurodevelopment. *Dev. Cell*. 48:873-882.e4.

Zhao, T., L. Guan, X. Ma, B. Chen, M. Ding, and W. Zou. 2022. The cell cortex-localized protein CHDP-1 is required for dendritic development and transport in C. elegans neurons. *PLoS Genet.* 18:e1010381.

Zou, W., X. Dong, T.R. Broederdorf, A. Shen, D.A. Kramer, R. Shi, X. Liang, D.M. Miller III, Y.K. Xiang, R. Yasuda, B. Chen, and K. Shen. 2018. A Dendritic Guidance Receptor Complex Brings Together Distinct Actin Regulators to Drive Efficient F-Actin Assembly and Branching. *Dev. Cell*. 45:362-375.e3.